

Mitochondrial iron chelation ameliorates cigarette smoke–induced bronchitis and emphysema in mice

Suzanne M Cloonan^{1,2}, Kimberly Glass^{3–5}, Maria E Laucho-Contreras², Abhiram R Bhashyam², Morgan Cervo⁶, Maria A Pabón¹, Csaba Konrad⁷, Francesca Polverino^{2,8,9}, Ilias I Siempos^{1,10}, Elizabeth Perez¹, Kenji Mizumura^{1,2}, Manik C Ghosh¹¹, Harikrishnan Parameswaran¹², Niamh C Williams¹, Kristen T Rooney¹, Zhi-Hua Chen^{2,13}, Monica P Goldklang^{14,15}, Guo-Cheng Yuan^{3,4}, Stephen C Moore⁶, Dawn L Demeo^{2,5}, Tracey A Rouault¹¹, Jeanine M D'Armiento^{14–16}, Eric A Schon^{17,18}, Giovanni Manfredi⁷, John Quackenbush^{3–5}, Ashfaq Mahmood⁶, Edwin K Silverman^{2,5}, Caroline A Owen^{2,8} & Augustine M K Choi^{1,2}

Chronic obstructive pulmonary disease (COPD) is linked to both cigarette smoking and genetic determinants. We have previously identified iron-responsive element–binding protein 2 (*IRP2*) as an important COPD susceptibility gene and have shown that IRP2 protein is increased in the lungs of individuals with COPD. Here we demonstrate that mice deficient in *Irp2* were protected from cigarette smoke (CS)-induced experimental COPD. By integrating RNA immunoprecipitation followed by sequencing (RIP-seq), RNA sequencing (RNA-seq), and gene expression and functional enrichment clustering analysis, we identified *Irp2* as a regulator of mitochondrial function in the lungs of mice. *Irp2* increased mitochondrial iron loading and levels of cytochrome *c* oxidase (COX), which led to mitochondrial dysfunction and subsequent experimental COPD. Frataxin-deficient mice, which had higher mitochondrial iron loading, showed impaired airway mucociliary clearance (MCC) and higher pulmonary inflammation at baseline, whereas mice deficient in the synthesis of cytochrome *c* oxidase, which have reduced COX, were protected from CS-induced pulmonary inflammation and impairment of MCC. Mice treated with a mitochondrial iron chelator or mice fed a low-iron diet were protected from CS-induced COPD. Mitochondrial iron chelation also alleviated CS-induced impairment of MCC, CS-induced pulmonary inflammation and CS-associated lung injury in mice with established COPD, suggesting a critical functional role and potential therapeutic intervention for the mitochondrial-iron axis in COPD.

COPD presents as a complex, debilitating lung disease that encompasses a variety of clinical and pathologic phenotypes ranging from airway inflammation (chronic bronchitis) to destruction of lung tissue (emphysema) and remodeling of the small airways^{1,2}. The pathogenesis of COPD remains poorly understood, but it involves aberrant inflammatory and dysregulated cellular responses of the lung to CS exposure¹.

CS exposure remains the greatest environmental risk factor for COPD; however, multiple studies have suggested that genetic factors also influence COPD susceptibility³. We previously identified *IRP2* (also known as *IREB2*) as a leading candidate COPD susceptibility gene^{4–6} in humans on the basis of genome-wide association studies

(GWAS), and we demonstrated that IRP2 protein is increased in the lungs of subjects with COPD⁴. *IRP2* is located within a cluster of genes on human chromosome 15q25, which includes genes that encode several components of the nicotinic acetylcholine receptor. In addition to COPD, 15q25 has been associated with lung cancer, peripheral arterial disease and nicotine addiction in GWAS^{7–10}.

The iron-regulatory proteins (IRPs) IRP1 and IRP2 regulate cellular iron homeostasis, with IRP2 serving as the major regulatory protein in mammalian cells¹¹. IRPs have important physiological roles in the duodenum, spinal cord and central nervous system, and in the pathogenesis of pulmonary hypertension and neurodegenerative diseases^{12–15}. In the setting of iron depletion, IRPs decrease iron

¹Joan and Sanford I. Weill Department of Medicine, New York–Presbyterian Hospital, Weill Cornell Medical College, New York, New York, USA. ²Division of Pulmonary and Critical Care Medicine, Brigham and Women's Hospital, Harvard Medical School, Boston, Massachusetts, USA. ³Department of Biostatistics, Harvard T.H. Chan School of Public Health, Boston, Massachusetts, USA. ⁴Department of Biostatistics and Computational Biology, Dana-Farber Cancer Institute, Boston, Massachusetts, USA. ⁵Channing Division of Network Medicine, Brigham and Women's Hospital, Harvard Medical School, Boston, Massachusetts, USA. ⁶Department of Radiology, Brigham and Women's Hospital, Harvard Medical School, Boston, Massachusetts, USA. ⁷Brain and Mind Research Institute, Weill Cornell Medical College, New York, New York, USA. ⁸Lovelace Respiratory Research Institute, Albuquerque, New Mexico, USA. ⁹Pulmonary Department, University of Parma, Parma, Italy. ¹⁰First Department of Critical Care Medicine and Pulmonary Services, Evangelismos Hospital, University of Athens Medical School, Athens, Greece. ¹¹Eunice Kennedy Shriver National Institute of Child Health and Human Development (NICHD), Bethesda, Maryland, USA. ¹²Department of Biomedical Engineering, Boston University, Boston, Massachusetts, USA. ¹³Department of Respiratory and Critical Care Medicine, Second Hospital of Zhejiang University School of Medicine, Hangzhou, China. ¹⁴Department of Anesthesiology, Columbia University, New York, New York, USA. ¹⁵Department of Medicine, Columbia University, New York, New York, USA. ¹⁶Department of Physiology & Cellular Biophysics, Columbia University, New York, New York, USA. ¹⁷Department of Neurology, Columbia University Medical Center, New York, New York, USA. ¹⁸Department of Genetics and Development, Columbia University Medical Center, New York, New York, USA. Correspondence should be addressed to A.M.K.C. (amc2056@med.cornell.edu).

Received 7 October 2015; accepted 1 December 2015; published online 11 January 2016; doi:10.1038/nm.4021

storage and increase iron uptake by binding to iron-response elements (IREs) located in the mRNAs of genes involved in iron homeostasis, which results in translational repression or stabilization of the transcripts^{12,15}. The critical physiological function of IRP2 in the lung and the mRNA transcripts targeted by IRP2 are not well known, nor is it clear whether IRP2 has a role in the response of the lung to CS exposure or in the pathogenesis of CS-induced COPD.

Here we sought to delineate the function of the COPD susceptibility gene *IRP2* in the pathogenesis of CS-induced COPD by integrating human COPD expression data with experimental mouse models of COPD. Our studies are the first to characterize a functional role for Irp2 in the lung, wherein Irp2 promotes mitochondrial dysfunction in experimental COPD by regulating mitochondrial iron loading and cytochrome *c* oxidase. Notably, we also show that mitochondrial iron chelation using the siderophore deferiprone alleviates established disease in a model of CS-induced pulmonary inflammation and injury (experimental COPD), highlighting a potential novel therapeutic approach for COPD.

RESULTS

Irp2-deficient mice resist experimental COPD

To characterize the functional role of IRP2 in the pathogenesis of COPD, we used two well-established experimental models of CS-induced COPD, namely CS-induced emphysema (4- to 6-month exposure)^{16,17} and CS-induced impairment of MCC (1-month exposure)^{17,18}. MCC, which is characterized by the upward movement of mucus by ciliary motion, can be impaired by airway-cell dysfunction¹⁹ or infiltration of immune cells into the lung²⁰. Impaired MCC leads to excessive airway mucus, recurrent pulmonary infection and chronic bronchitis¹.

Consistent with our observations from the lungs of human subjects with COPD⁴, we observed higher Irp2 expression (with no change in Irp1 expression) and activity in the lungs of wild-type (WT) mice exposed to CS for 1–6 months as compared to room air (RA)-exposed controls (Fig. 1a–c). Irp2 expression was localized in lung epithelial cells, including type I alveolar (podoplanin-positive), type II alveolar (prosurfactant protein C (SPC)-positive), secretory airway (uteroglobin-positive) and ciliated airway (acetylated α -tubulin-positive) cells (Fig. 1d and Supplementary Fig. 1a,b), as assessed by immunohistochemical analyses. Irp2 expression also seemed to localize to the walls of intermediate-size vessels, with negligible staining in basal (cytokeratin 5-positive) epithelial cells (Supplementary Fig. 1b). Irp2 expression was higher in type I, type II, secretory and ciliated epithelial cells, as well as in infiltrating alveolar macrophages in response to CS (6-month exposure), as compared to RA controls (Fig. 1d and Supplementary Fig. 1a,b). We also observed higher Irp2 expression after aqueous cigarette-smoke extract (CSE) treatment (an *in vitro* model of CS exposure) in primary human bronchial airway epithelial cells and in the human bronchial airway epithelial cell line Beas2B, as compared to RA-exposed controls (Supplementary Fig. 1c,d).

Overexpression of Irp2 has been associated with embryonic lethality in mice²¹; we therefore used a loss-of-function approach to study the function of Irp2 in experimental COPD. WT mice exposed to CS for 4–6 months had increased mean chord lengths and air-space diameters (Fig. 1d and Supplementary Fig. 2a), and showed greater thickness of the small airways (all established indices of experimental COPD^{2,17}), as compared to RA-exposed WT mice (Fig. 1e). *Irp2*^{-/-} mice resisted CS-induced changes in mean chord length and air-space diameter and were protected from small-airway remodeling (Fig. 1e,f and Supplementary Fig. 2a). *Irp2*^{-/-} mice were also protected from

the expression of CS-induced injury markers previously shown to be associated with emphysema, including cleaved caspase-3 (indicating increased apoptosis)²², matrix metalloproteinase 9 (MMP9)²³ expression and the autophagy markers LC3B¹⁷ and Atg7 (Fig. 1g and Supplementary Fig. 2b,c). Irp1 expression did not change in RA- or CS-exposed *Irp2*^{-/-} mice (Supplementary Fig. 2d).

We have recently developed an experimental model of CS-induced bronchitis by exposing mice acutely to CS (1-month exposure) and measuring MCC^{17,18} (Fig. 1h). In this model, bronchoalveolar lavage (BAL) fluid (BALF) from CS-exposed WT mice had greater leukocyte counts and greater total BALF protein levels (an indicator of increased epithelial cell injury and permeability²⁴) than RA-exposed WT mice (Supplementary Fig. 2e,f). CS-exposed mice also had higher concentrations of BALF interleukin (IL)-33 (a pleiotropic cytokine predominantly expressed in lung tissue that induces airway inflammation in naive mice²⁵) and BALF IL-6 (a cytokine associated with the severity of acute COPD exacerbations and decline in lung function²⁶) than RA-exposed WT mice (Fig. 1i). Using this model, the MCC of WT lungs exposed to CS was significantly lower than that of RA-exposed controls ($P < 0.05$) (Fig. 1h). *Irp2*^{-/-} mice were protected from CS-impaired MCC, and CS-exposed *Irp2*^{-/-} mice exhibited less BALF IL-6 and IL-33 than CS-exposed WT mice (Fig. 1h,i). Irp2 deficiency failed to protect against lung injury (with increased numbers of BAL leukocytes and increased levels of BALF protein and BAL IL-6 and IL-33 protein) and mortality in a hyperoxia-induced acute lung injury mouse model and in a cecal ligation and puncture-induced polymicrobial sepsis mouse model (Supplementary Fig. 3a–g), highlighting the specificity of the functional role of IRP2 in CS-induced lung injury associated with COPD.

Identification of novel target pathways of IRP2 in the lung

As described above, Irp2 conferred important functional impacts in the pathogenesis of COPD in two experimental COPD models. We therefore sought to delineate the mechanism by which Irp2 promoted experimental COPD by first identifying the downstream targets of IRP2 in the lung. For unbiased identification of RNA targets of IRP2, we used the human airway epithelial cell line Beas2B, either stimulated with deferoxamine (DFO) (to stabilize IRP2 expression²⁷) or left unstimulated, immunoprecipitated IRP2-RNA complexes and performed whole-transcriptome sequencing (RIP-seq) (Supplementary Fig. 4a–c). This analysis identified 1,806 IRP2-related target genes, which included transcripts for known IRP2 targets, such as ferritin and the transferrin receptor (TfR) (Supplementary Fig. 4d–f), thus validating the model system.

To better understand the biological meaning behind the IRP2 target genes, we used functional enrichment clustering analysis (see Online Methods and Supplementary Fig. 4g) and identified five core functional ‘communities’ or pathways (depicted as word clouds), as demonstrated by the Circos plot in Figure 2a. On this plot, the differential expression of genes in the lung tissue of individuals with COPD (from the Lung Genomics Research Consortium (LGRC)), as compared to that of healthy controls (black ring), is also shown (Fig. 2a). We observed that many of the genes in each of the five communities had altered expression in subjects with COPD and were known to be involved in the progression or pathogenesis of COPD (Supplementary Table 1).

To associate this human data to the heterogeneous *in vivo* environment of the lung in the absence of IRP2, we evaluated each of the five RIP-seq-derived communities for differential expression patterns using a microarray study of lungs from WT and *Irp2*^{-/-} mice (Fig. 2b).

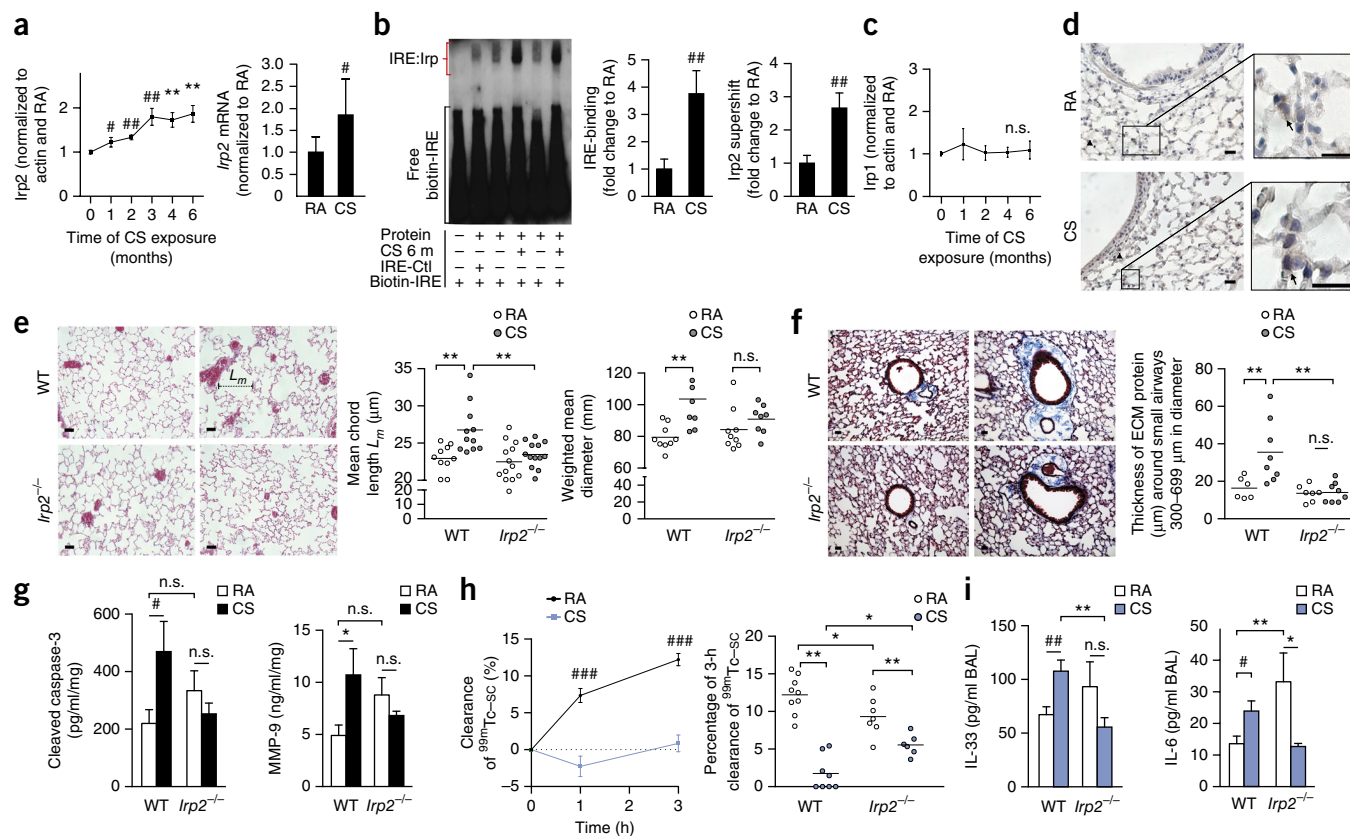


Figure 1 *Irf2* is pathogenic in experimental COPD. **(a)** Quantification of *Irf2* protein in WT mouse lungs exposed to room air (RA) or CS (1–6 months) (left) and *Irf2* mRNA (at 6 months; right) levels ($n = 8$ per group). **(b)** Representative ($n = 4$) electrophoretic mobility shift assay (EMSA) (left) and quantification (middle and right) of total *Irf1* (middle; $n = 5$ per group) or *Irf2* (right; $n = 3$ per group) activity. **(c)** *Irf1* protein expression in WT mouse lungs exposed to RA or CS (1–6 months) ($n = 3$ per group). **(d)** Representative micrographs for *Irf2* immunostaining (arrows indicate *Irf2*) in WT mouse lungs exposed to RA (top) or CS (bottom) for 1–6 months. Lower-magnification images (left) and higher-magnification images of boxed areas (right) are shown. Scale bars, 50 μm . **(e)** Left, representative H&E-stained lung sections ($n = 3$ mice per group) of WT (top) and *Irf2*^{-/-} (bottom) mice exposed to RA (left) or CS (right) for 6 months. Scale bars, 50 μm . Middle and right, quantification of mean chord length L_m (middle) and weighted mean diameters (right) of RA- or CS-exposed (6 months) WT and *Irf2*^{-/-} mice. **(f)** Left, representative micrographs ($n = 2$ technical replicates) of trichrome-stained lung sections from WT (top) and *Irf2*^{-/-} (bottom) mice exposed to RA (left) or CS (right). Scale bars, 50 μm . Right, quantification of the thickness of extracellular matrix (ECM) protein around the small airways in WT and *Irf2*^{-/-} mice exposed to RA or CS for 6 months. **(g)** Quantification of cleaved caspase-3 (picograms of cleaved caspase-3 per milliliter per milligram of lung tissue) ($n = 7$ per group) (left) and MMP-9 (WT: RA, $n = 5$; CS, $n = 3$; *Irf2*^{-/-}: RA, $n = 6$; CS, $n = 6$) (right) levels in whole lungs of WT and *Irf2*^{-/-} mice exposed to RA or CS for 6 months, using ELISA ($n = 2$ technical replicates). **(h)** ^{99m}Tc-sc clearance over 1–3 h (left) in WT mouse lungs exposed to RA ($n = 9$) or CS ($n = 10$) for 1 month. 3 h ^{99m}Tc-sc clearance (right), **(i)** BALF IL-33 (left, ELISA; WTRA $n = 3$; WTCS $n = 5$; *Irf2*^{-/-} RA $n = 5$; *Irf2*^{-/-} CS $n = 6$) and BALF IL-6 protein concentrations (right, ELISA, $n = 3$ per group) in WT and *Irf2*^{-/-} mice exposed to RA or CS (1 month). Throughout, data are mean \pm s.e.m. * $P < 0.05$, ** $P < 0.01$ by one-way analysis of variance (ANOVA) with Bonferroni correction; # $P < 0.05$, ## $P < 0.01$, ### $P < 0.005$ by Student's unpaired *t*-test; n.s., not significant.

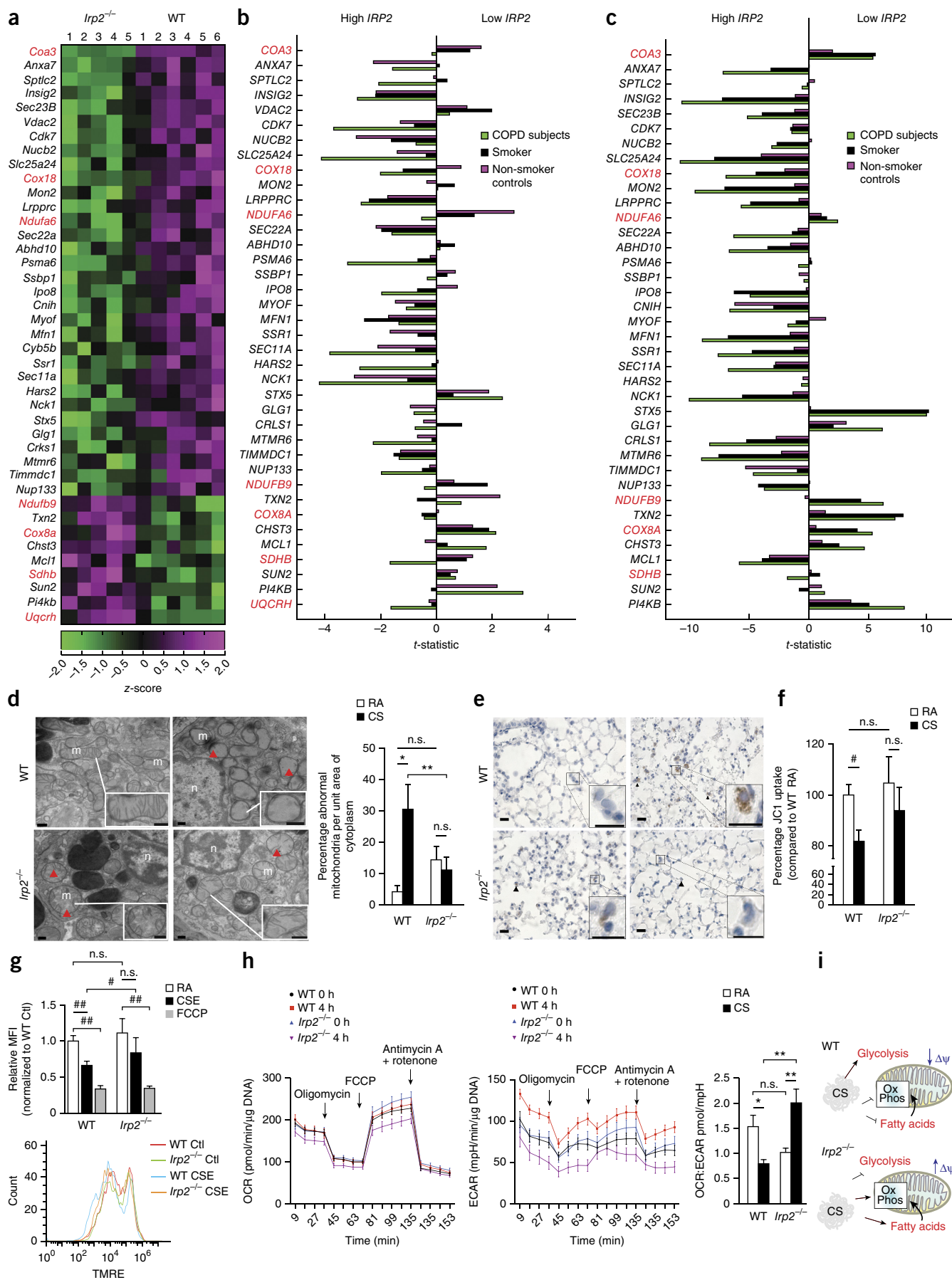
This analysis identified one community, community 2, as having the most significant differential expression of genes between the *Irf2*^{-/-} and WT mice (Fig. 2c) ($P = 1.08 \times 10^{-8}$). Gene Ontology database analysis of the differentially expressed genes associated with community 2 (Fig. 3a and Supplementary Fig. 5) showed that one of the main pathways to emerge was related to mitochondrial function.

To assess the relationship between the differentially expressed mitochondrial genes (Fig. 3a) and *IRP2* expression in human subjects with COPD, we evaluated the expression pattern of these genes in individuals with COPD and in control individuals with high or low *IRP2* expression using two human COPD cohorts, namely the LGRC (gene expression in lung tissue) and ECLIPSE (evaluation of COPD longitudinally to identify predictive surrogate end points; gene expression in blood) cohorts. A strong association between the differential expression of mitochondrial genes and differences in *IRP2* expression were

observed, with an overall stronger association observed in subjects with COPD (Fig. 3b,c and Supplementary Fig. 6).

Irf2^{-/-} mice resist CS-induced mitochondrial dysfunction

On the basis of the functional pathways highlighted in the RIP-seq and differential-expression analyses from mice and humans, we assessed the functional role of *IRP2* in mitochondrial responses to CS in experimental COPD. We found that lung epithelial cells from WT mice exposed to CS had abnormal mitochondrial morphology, with evidence of cristae loss and mitochondrial swelling (Fig. 3d). *Irf2*^{-/-} mice had higher levels of abnormal mitochondrial morphology at baseline, as compared to WT controls, and in response to CS, *Irf2*^{-/-} mouse airway cells developed fewer mitochondria with abnormal morphology (Fig. 3d). Immunohistochemical staining for cytosolic cytochrome *c*, a marker of mitochondrial damage²⁸, demonstrated that CS-induced mitochondrial damage localized to alveolar and



relative negative charge (Fig. 3g). Human airway epithelial cells deficient in IRP2 (as a result of treatment with short interfering RNA (siRNA) specific for *IRP2*) were protected from CSE-induced cell death and from the production of CSE-induced mitochondrial reactive oxygen species (mtROS)¹⁷ (Supplementary Fig. 8a,b). Taken together, these data implicate IRP2 as a regulator of CS-induced mitochondrial dysfunction in experimental COPD.

Using a Seahorse XF96 apparatus, which provides information on mitochondrial function through real-time measurements of oxygen consumption rate (OCR; a marker of oxidative phosphorylation (OxPhos)) and extracellular acidification (ECAR; a surrogate for glycolysis), we determined the rates and reserve capacity of OxPhos and glycolytic activity in CSE-exposed WT and *Irp2*^{-/-} primary lung epithelial cells (Fig. 3h). CSE-exposed WT cells had lower OCR:ECAR ratios than RA-exposed cells, indicative of cells shifting energy metabolism from OxPhos to glycolysis. CSE-exposed *Irp2*^{-/-} cells had the opposite response in OCR:ECAR ratio, which was characterized by greater levels of OxPhos relative to glycolysis, indicative of enhanced aerobic mitochondrial metabolism with less reliance on glycolysis (Fig. 3h). These results suggest that, in lung epithelial cells, IRP2 regulates switching from aerobic (OxPhos) to anaerobic metabolism as an adaptive response to mitochondrial dysfunction (Fig. 3i).

IRP2 promotes CS-induced mitochondrial iron loading

Mitochondria are the main consumers of intracellular iron, and a number of vital cellular processes rely on precise mitochondrial iron regulation²⁹. Failure to control mitochondrial iron levels leads to mitochondrial iron loss or excessive mitochondrial iron overload, both of which can lead to mitochondrial dysfunction²⁹. We wished to investigate whether the observed IRP2-mediated mitochondrial responses to CS (Fig. 3d–h) were related to IRP2-mediated alterations in mitochondrial iron pathways in the lung.

We first investigated whether CS regulated general iron metabolism in the lung. In body tissues, iron (Fe) is found either as non-heme free iron in the ferric (Fe³⁺) or ferrous (Fe²⁺) state or as heme iron (Fe²⁺ complexed with protoporphyrin IX)³⁰. Consistent with greater *Irp2* expression in CS-exposed WT mice, WT mice had higher non-heme iron in inflated lung sections and in whole-lung homogenates than RA-exposed mice (Fig. 4a). Whole-lung homogenates of WT mice also had higher and lower expression of the *Irp2* target proteins TfR and ferritin, respectively (Fig. 4b). Additionally, intracellular free iron was higher in human airway epithelial cells after exposure to aqueous CSE as compared to RA (Supplementary Fig. 8a). These data suggested that in experimental models of COPD, CS exposure increased iron deposition in the airways of mice. CS-exposed *Irp2*^{-/-} mice had similar total non-heme iron levels in whole lung tissue, as compared to CS-exposed WT mice (Fig. 4c); however, staining with Perls' Prussian Blue, which detects ferric iron deposits, revealed less iron deposition in CS-exposed *Irp2*^{-/-} mouse lungs than in CS-exposed WT mouse lungs (Supplementary Fig. 8b). Furthermore, intracellular free iron levels did not change in CSE-exposed human airway epithelial cells deficient in IRP2 (by treatment with a short hairpin RNA (shRNA) targeting *IRP2*) (Supplementary Fig. 8a).

Once inside the cell, free iron may be delivered to ferritin³⁰ and iron-containing proteins, or it may be imported into mitochondria for heme or iron-sulfur (Fe-S) cluster biosynthesis. Non-heme and heme iron levels were higher in mitochondrial fractions of WT mouse lungs exposed to CS, as compared to those from RA-exposed controls (Fig. 4c,d). Increased mitochondrial iron import is reliant on the use of the inner mitochondrial membrane iron transporter

mitoferrin 2 (ref. 31). Mitoferrin 2 levels were higher in CS-exposed mice than in RA-exposed controls (Fig. 4e), suggesting increased import of iron into mitochondria. Another indicator of increased iron loading, loss of the mitochondrial Fe-S regulator frataxin³², was also associated with CS exposure in whole-lung homogenates of WT mice as well as in human airway epithelial cells treated with CSE (Fig. 4f and Supplementary Fig. 8c). Ferritin expression was lower in lung tissue from CS-exposed mice than in tissue from RA-exposed mice, but the expression of cytosolic non-heme and heme iron and of the cytosolic iron-binding protein F-box and leucine-rich repeat protein 5 (Fbxl5, also a negative regulator of *Irp2* (ref. 21)) was unchanged (Supplementary Fig. 8d–f). Additionally, CSE treatment impaired mitochondria and cytosolic Fe-S cluster assembly in human airway epithelial cells (Supplementary Fig. 8g). Taken together, these data demonstrate that exposure to CS induced mitochondrial iron loading in experimental COPD.

Irp2^{-/-} mice were protected from the effects of CS on ferritin and mitoferrin 2 expression, as compared to CS-exposed WT mice (Fig. 4d,e and Supplementary Fig. 8d). *Irp2*^{-/-} mice were also protected from CS-associated higher mitochondrial non-heme iron and mitochondrial heme iron levels (Fig. 4d), suggesting that IRP2 promoted CS-induced mitochondrial iron loading. We have previously shown that heme oxygenase 1 (HO-1), an enzyme that catalyzes the degradation of heme to produce iron, is elevated in CS-exposed mouse lungs and that it may have a protective role in regulating CS-induced mitochondria-mediated cell death³³. Here we show that the lungs of *Irp2*^{-/-} mice had higher baseline levels of HO-, which did not change after CS exposure, than did CS-exposed WT mice (Supplementary Fig. 8h), suggesting that the *Irp2*^{-/-} mice have more baseline protection from mitochondria-mediated cell death.

To assess whether abnormally increased mitochondrial iron overload is pathogenic in experimental COPD, we evaluated whether mice with higher mitochondrial iron loading (i.e., mice with reduced frataxin expression³²) had differential responses to CS exposure in our CS-induced impairment of MCC (bronchitis) mouse model. We chose to use this acute 1-month exposure model to test our hypothesis, as we observed significant differences ($P < 0.05$) in CS-induced mitochondrial iron loading between WT and *Irp2*^{-/-} mice at this time point (Fig. 4d). Here we found that mice deficient in frataxin (i.e., mice with a heterozygous transgenic insertion (GAA₂₃₀ expansion) of mutated frataxin (knock-in, ki) and a heterozygous deletion of frataxin (knockout, ko); *Fxn*^{ki/ko} mice) had higher mitochondrial non-heme and heme iron levels, significantly impaired baseline MCC function ($P < 0.05$) and higher baseline levels of whole-lung IL-6 protein (Fig. 4g,h) as compared to WT mice. These data suggest that CS-induced mitochondrial iron loading may be pathogenic in experimental COPD models (Fig. 4i).

IRP2 and CS increased lung COX activity and expression

To investigate the mechanism of IRP2-associated mitochondrial iron loading and CS-induced mitochondrial dysfunction, we focused our attention to the mitochondrial genes identified in our RIP-seq study and community-based gene expression analysis (Fig. 3a). The most significant differentially expressed gene ($P < 0.01$) in this analysis was COX assembly factor 3 (*Coa3*), which was expressed at lower levels in *Irp2*^{-/-} mice than in WT mice (Figs. 3a and 5a). *Coa3* encodes coiled-coil domain-containing protein 56 (CCDC56), a mitochondrial protein that stabilizes COX subunit I and promotes its assembly and activity³⁴ (Fig. 5a). COX is the terminal electron acceptor of the mitochondrial electron transport chain and is responsible for the

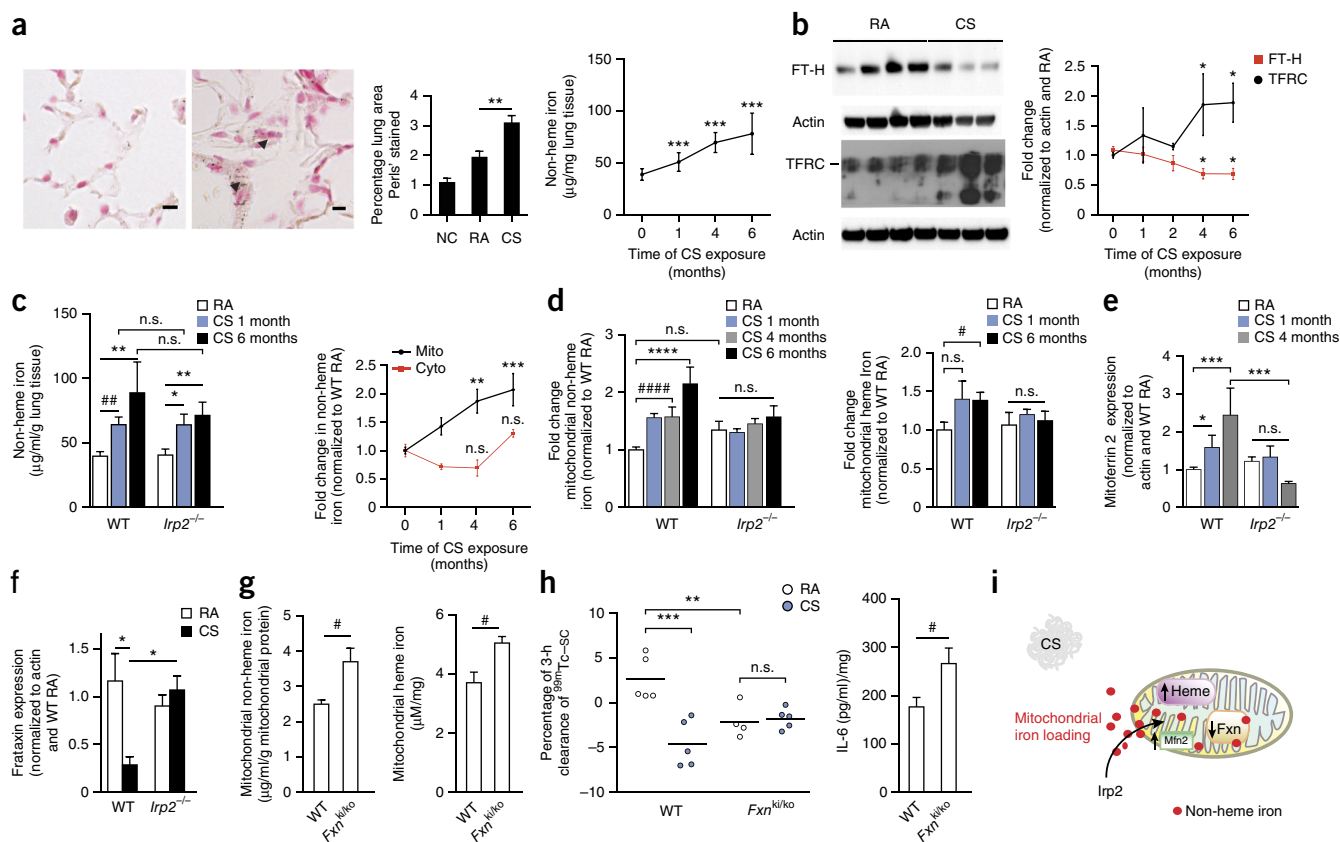


Figure 4 IRP2-associated mitochondrial-iron loading and CS exposure. **(a)** Left, representative micrographs of Perls'-stained lung sections ($n = 3$ mice per group; $n = 2$ technical replicates) from WT mice exposed to RA (left) or CS (right) for 1–6 months (6-month time point is shown). Arrowheads indicate staining. Scale bars, 50 μm . Middle and right, quantification of Perls'-stained lung areas at 6 months ($n = 10$ images per mouse; $n = 3$ per group) (middle) and non-heme iron levels (right; $n = 4$ mice per group; $n = 4$ technical replicates) in WT mice exposed to RA or CS for 1–6 months. NC, negative control. **(b)** Representative immunoblot analysis ($n = 3$ experiments) (left) and quantification (right) of transferrin receptor (TFRC) and ferritin heavy chain (FT-H) expression in WT mouse lungs exposed to RA or CS ($n = 5$ per group; $n = 2$ technical replicates). Actin was used as a loading control. **(c)** Quantification of total non-heme iron ($n = 5$ mice per group; $n = 4$ technical replicates) (left) and fold changes in mitochondrial (mito) (RA, $n = 11$; CS (1 month), $n = 6$; CS (4 months), $n = 8$; CS (6 months), $n = 9$) and cytosolic (cyto) (RA, $n = 6$; CS (1 month), $n = 11$; CS (4 months), $n = 3$; CS (6 months), $n = 5$) non-heme iron (right) in WT mouse lungs exposed to RA or CS ($n = 2$ technical replicates). **(d)** Quantification of fold changes in non-heme iron (for WT and *Irp2*^{-/-} mice: RA, $n = 13$; CS (1 month), $n = 5$; CS (4 months), $n = 3$; CS (6 months), $n = 3$) (left) and heme iron (for WT and *Irp2*^{-/-}; RA, $n = 10$, CS-exposed, $n = 5$ per group) (right) in mitochondrial fractions from mouse lungs exposed to RA or CS ($n = 2$ technical replicates). **(e)** Quantification of mitoferrin 2 (Mfn2) expression in whole lungs of mice (for WT and *Irp2*^{-/-}: RA, $n = 8$; CS (1 month), $n = 3$; CS (4 months), $n = 6$) after exposure to RA or CS. **(f)** Quantification of frataxin protein expression in whole lungs of mice exposed to RA or CS for 6 months (WT: RA, $n = 5$; CS, $n = 3$; *Irp2*^{-/-}: RA, $n = 6$; CS, $n = 6$). **(g,h)** Quantification of mitochondrial non-heme iron ($n = 4$ per group) (g, left), mitochondrial heme iron ($n = 4$ per group) (g, right), 3-h ^{99m}Tc-SC clearance (h, left; each circle represents a single mouse, and horizontal lines denote mean) and IL-6 protein concentrations ($n = 4$ per group) (h, right) in the lungs of WT and *Fxn*^{ki/ko} mice exposed to RA or CS for 1 month. **(i)** Schematic of regulation of mitochondrial iron loading by *Irp2*. Throughout, data are mean \pm s.e.m. * $P < 0.05$, ** $P < 0.01$, *** $P < 0.005$, **** $P < 0.001$ by one-way ANOVA followed by Bonferroni correction; # $P < 0.05$, ## $P < 0.01$, ### $P < 0.001$ by Student's unpaired *t*-test; n.s., not significant.

conversion of oxygen into water. A number of genes encoding other subunits and factors important for COX assembly (such as *Cox18* and *Cox8A*) and mitochondrial OxPhos (including NADH dehydrogenase (ubiquinone) 1 (Nduf) alpha subcomplex, 6 (*Nduf66*) and Nduf beta subcomplex, 9 (*Nduf9*) (complex I), succinate dehydrogenase complex, subunit B, iron sulfur (*Sdhb*) (complex II) and ubiquinol-cytochrome *c* reductase hinge protein (*Uqcrc*) (complex III)) were also differentially expressed in *Irp2*^{-/-} versus WT mice according to this analysis, in addition to other proteins important for mitochondrial integrity and apoptosis (Fig. 3a).

It has been proposed that COX acts as a key regulator of mitochondrial iron metabolism³⁵. Specifically, COX subunit I is regulated by heme and is the site of iron reduction and transport into mitochondria³⁵, where it supplies iron for heme biosynthesis³⁵. Consistent

with higher *Irp2* expression and with altered expression of COX-related mitochondrial genes in WT as compared to *Irp2*^{-/-} mice (Figs. 3a and 5a), we found that COX expression is higher in lung biopsies from individuals with COPD than in those from control subjects (Fig. 5a).

Using an antibody that detects each complex of the mitochondrial electron transport chain, we observed that COX expression was higher in lungs from CS-exposed WT mice than in lungs from CS-exposed *Irp2*^{-/-} mice (Fig. 5b). *Irp2*^{-/-} mouse lungs also exhibited less CS-induced reduction in the expression of complexes I and II (Supplementary Fig. 9a). Expression of the lung-specific isoform of COX (*Cox4i2*), which renders lung COX twofold more active than COX in other tissues that lack *Cox4i2* (ref. 36), was also higher in CS-exposed WT mice. *Irp2*^{-/-} mice had lower *Cox4i2* expression than

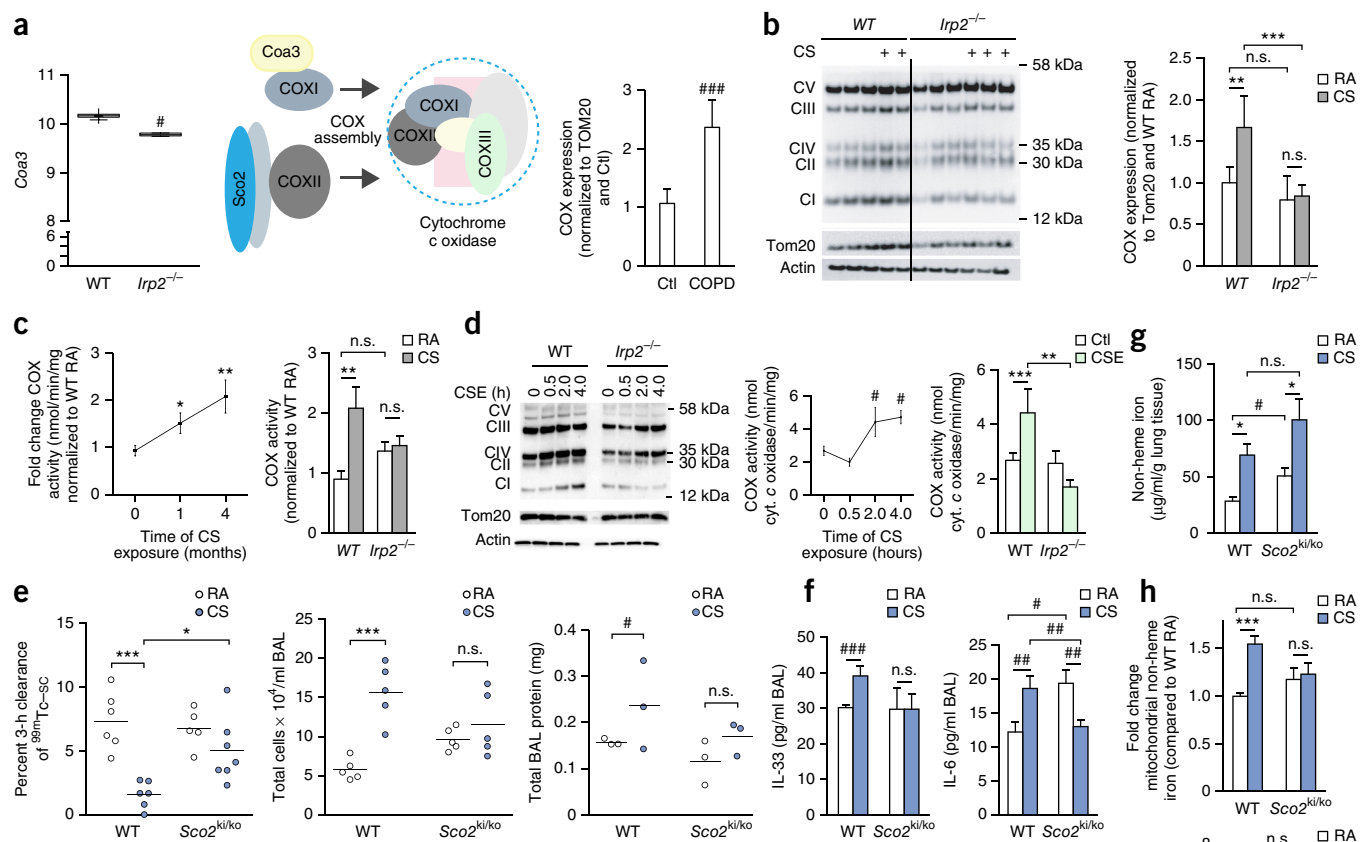


Figure 5 COX is pathogenic in experimental COPD. **(a)** *Coa3* expression in WT ($n = 6$) and *Irp2*^{-/-} ($n = 5$) mouse lungs (left) (robust multiarray average (RMA) normalized), schematic of COX assembly (middle) and COX expression in lung tissue from individuals with COPD ($n = 5$) and controls ($n = 5$) by immunoblot analysis (right) ($n = 2$ technical replicates). **(b)** Representative immunoblot analysis ($n = 3$ experiments) of OxPhos complexes I–V (CI–CV) in mitochondria-enriched fractions from WT and *Irp2*^{-/-} mouse lungs exposed to RA or CS for 4 months (left) and quantification of complex IV expression ($n = 3$ technical replicates) (right). **(c)** Quantification of changes in COX activity over time (left) and total COX activity after 4 months of CS exposure in mitochondrial fractions of WT and *Irp2*^{-/-} mice exposed to RA or CS ($n = 3$ per group; $n = 3$ technical replicates). **(d)** Representative immunoblot analysis ($n = 3$ experiments) as in **b** (left), time course of COX activity (middle) and COX activity after 4 h of exposure (right) in primary lung epithelial cells from WT or *Irp2*^{-/-} mice exposed to 20% CSE ($n = 2$ per group; $n = 2$ technical replicates). **(e)** Quantification of 3-h ^{99m}Tc-sc clearance (left), total BALF leukocytes (middle) and total BALF protein levels (right) in WT and *Sco2*^{ki/ko} mice exposed to RA or CS for 1 month. Each circle represents one mouse, and horizontal lines denote mean. **(f)** Quantification of BALF IL-33 (WT: RA, $n = 4$; CS, $n = 5$; *Sco2*^{ki/ko}: RA, $n = 5$; CS, $n = 4$) and BALF IL-6 (WT: RA, $n = 4$; CS, $n = 5$; *Sco2*^{ki/ko}: RA, $n = 5$; CS, $n = 4$) levels for 1 month, using ELISA ($n = 3$ technical replicates). **(g)** Quantification of total lung non-heme iron ($n = 4$ per group) ($n = 3$ technical replicates), mitochondrial non-heme iron ($n = 3$ per group) (**h**, left) and mitochondrial heme iron ($n = 3$ per group) (**h**, right) levels in WT and *Sco2*^{ki/ko} mice exposed to RA or CS for 1 month. **(i)** Schematic of the role of COX *Irp2*-associated mitochondrial iron loading. Throughout, data are mean \pm s.e.m. * $P < 0.05$, ** $P < 0.01$, *** $P < 0.005$ by one-way ANOVA followed by Bonferroni correction; # $P < 0.05$, ## $P < 0.01$, ### $P < 0.005$ by unpaired Student's *t*-test; n.s., not significant.

WT mice, which did not change after exposure to CS (**Supplementary Fig. 9b**). Similarly, COX activity was higher in mitochondrial fractions isolated from WT mice that were exposed to CS for 1 month and 4 months, as compared to those from RA-exposed control mice (**Fig. 5c**). COX activity was also higher in mitochondria from CS-exposed WT mouse lungs, but it did not change in mitochondria from CS-exposed *Irp2*^{-/-} mouse lungs (**Fig. 5c**). Additionally, CSE-exposed WT lung epithelial cells had greater COX expression and activity than CSE-exposed airway epithelial cells from *Irp2*^{-/-} mice (**Fig. 5d**).

To examine the function of COX in the response of the lung to CS, we used mice with impaired COX (activity and expression) in our CS-induced bronchitis model. COX is a multi-subunit complex whose assembly requires >20 ancillary factors including that encoded by

'synthesis of cytochrome *c* oxidase' (*SCO2*)³⁷ (**Fig. 5a**). By using serial analysis of gene expression (SAGE), we previously showed that *SCO2* expression is higher in the lungs of subjects with COPD as compared to the lungs of healthy smokers and non-smokers³⁸. Homozygous deletion of *Sco2* is embryonic lethal in mice³⁷; however, mice harboring either a *Sco2* ki mutation on one allele and a deletion (ko) of *Sco2* on the other allele, or two ki mutations, have COX assembly defects and impaired COX activity (with *Sco2*^{ki/ko} mice showing more severe COX deficiency than *Sco2*^{ki/ki} mice³⁷). We assessed the MCC of *Sco2*^{ki/ko} and *Sco2*^{ki/ki} mice that were exposed acutely to CS. WT mice had impaired MCC, higher BAL leukocyte counts and higher total BALF protein levels (**Fig. 5e** and **Supplementary Fig. 9c,d**). Conversely, *Sco2*^{ki/ko} and *Sco2*^{ki/ki} mice were protected from

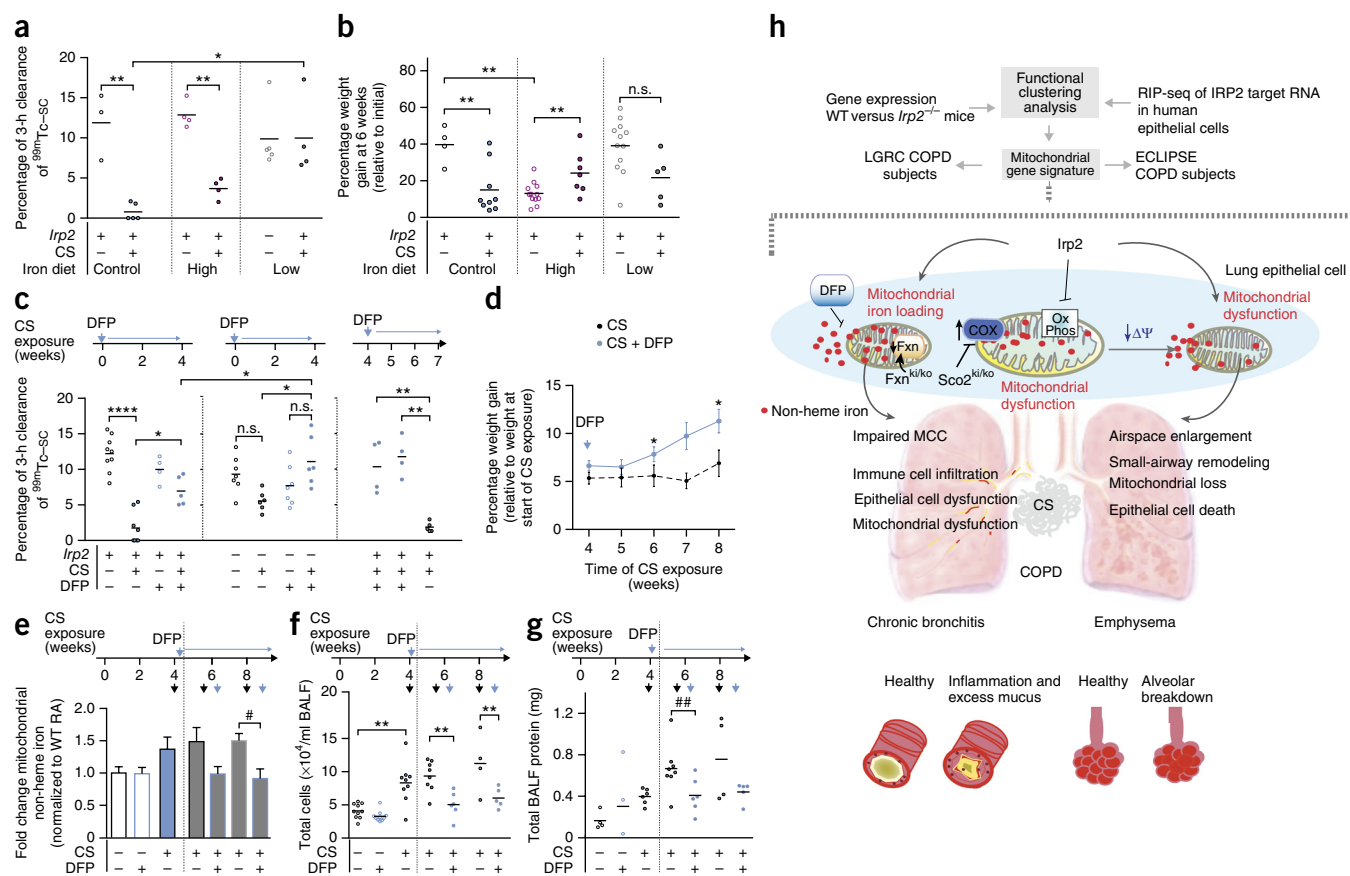


Figure 6 Targeting mitochondrial iron in experimental COPD. **(a,b)** Quantification of 3-h $^{99m}\text{Tc-sc}$ clearance **(a)** and weight gain in WT mice that were exposed to RA or CS for 1 month and on a control (300-p.p.m. iron), low-iron (6 p.p.m. iron) or high-iron (2% carbonyl iron) diet. Each circle represents a mouse, and horizontal lines denote mean. **(c)** Quantification of 3-h $^{99m}\text{Tc-sc}$ clearance in WT and *Irp2*^{-/-} mice exposed to RA or CS for 1 month and treated with DFP either as a prophylactic dosing strategy or as a therapeutic dosing strategy (blue arrows indicate time of DFP addition). **(d)** Quantification of weight gain in WT mice over time after CS exposure (relative to initial weight at the start of CS exposure) in the absence (black dashed line; CS only: 4 weeks, $n = 17$; 5 weeks, $n = 12$; 6 weeks, $n = 12$; 7 weeks, $n = 4$; 8 weeks, $n = 4$) or presence of DFP (administered after 4-week CS exposure (indicated by blue arrow) and continued for the duration of CS exposure) (blue line; CS (4 weeks) + DFP: 4 weeks, $n = 11$; 5 weeks, $n = 11$; 6 weeks, $n = 11$; 7 weeks, $n = 5$; 8 weeks, $n = 4$). **(e-g)** Quantification of changes in lung mitochondrial non-heme iron levels (control, $n = 8$; DFP control $n = 8$; CS (1 month), $n = 10$; CS (6 weeks), $n = 4$; CS + DFP (6 weeks) $n = 4$; CS (8 weeks) $n = 4$; CS + DFP (8 weeks), $n = 4$; $n = 2$ technical replicates) **(e)**, total numbers of BAL leukocytes **(f)** and total BALF protein levels in WT mice treated with DFP using the therapeutic dosing strategy described in **c** but continued for an additional 2 or 4 weeks of CS exposure. Black arrows indicate time of CS exposure and blue arrows indicate time of DFP addition. **(h)** Schematic of the major findings of this study. Throughout, data are mean \pm s.e.m. * $P < 0.05$, ** $P < 0.01$, **** $P < 0.001$ by one-way ANOVA followed by Bonferroni correction. # $P < 0.05$, ## $P < 0.01$ by Student's unpaired t -test; n.s., not significant.

CS-induced loss of MCC (with *Sco2*^{ki/ko} showing greater protection than *Sco2*^{ki/ki} mice) (Fig. 5e and Supplementary Fig. 9c). CS-exposed *Sco2*^{ki/ko} mice exhibited lower total BALF levels of IL-6 and IL-33 and lower BAL leukocyte counts than CS-exposed WT mice (Fig. 5f and Supplementary Fig. 9d), supporting the hypothesis that increased COX activity confers pathogenicity in experimental COPD.

To determine whether loss of COX resulted in higher levels of mitochondrial iron in a manner similar to that observed with the loss of *Irp2*, we measured total-lung tissue non-heme iron levels, as well as cytosolic and mitochondrial iron (non-heme and heme) levels, in WT and *Sco2*^{ki/ko} mouse lungs exposed to RA or CS (for 1 month). Consistent with the results obtained in WT mice, CS-exposed WT mice had higher total-lung non-heme iron levels as well as higher mitochondrial non-heme and heme iron levels than RA-exposed WT mice (Fig. 5g,h). Similarly to the *Irp2*^{-/-} mice, *Sco2*^{ki/ko} mice were protected from CS-associated changes in mitochondrial non-heme iron (Figs. 4d and 5h). No difference in mitochondrial heme levels or in cytosolic non-heme and heme iron

levels was observed in RA- or CS-exposed *Sco2*^{ki/ko} mice, as compared to those from WT mice (Fig. 5h and Supplementary Fig. 9e,f). These data suggested that *Irp2* increased COX, which may be associated with altered mitochondrial non-heme iron in experimental COPD (Fig. 5i).

Targeting mitochondrial iron in experimental COPD

To test the hypothesis that *Irp2* increases mitochondrial iron loading, which leads to mitochondrial dysfunction in experimental COPD, we first assessed whether modulating iron in the diets of WT mice altered responses to CS exposure in our CS-induced bronchitis model. Mice fed a low-iron diet had lower serum and lung non-heme iron levels and were protected from CS-induced MCC impairment (with no effect on weight gain) as compared to mice fed a control iron-replete diet (Fig. 6a,b and Supplementary Fig. 10a). Mice fed a high-iron diet had higher serum and lung non-heme iron levels, as compared to mice fed a control iron-replete diet, and they showed impaired weight gain at baseline but exhibited similar mucociliary responses

to CS exposure as mice fed a control iron-replete diet (Fig. 6a,b and Supplementary Fig. 10a).

We next examined whether alleviating excess mitochondrial iron would alter responses to CS exposure in our CS-induced bronchitis model. Deferiprone (DFP or ferriprox) is an iron chelator that specifically targets mitochondrial non-heme iron deposits and relocates them elsewhere to prevent mitochondrial iron loading^{39,40}. Administration of DFP for the duration of CS exposure protected mice from CS-induced MCC impairment (Fig. 6c). The protection afforded by DFP treatment was similar to that observed in the *Irp2*^{-/-} mice. Administering DFP in an *Irp2*-deficient background showed synergistic effects, i.e., DFP-treated *Irp2*^{-/-} mice had better protection from CS-induced MCC impairment than DFP-treated WT mice or *Irp2*^{-/-} mice (Fig. 6c).

Finally, we evaluated whether mitochondrial iron chelation could alleviate established experimental COPD (pulmonary inflammation and injury) when administered as a therapeutic dosing strategy. WT mice with existing impaired MCC (which develops after 4 weeks of CS exposure) that were treated with DFP during an additional 1.5 or 3 weeks of CS exposure had significantly improved mucociliary clearance ($P < 0.05$), as compared to mice exposed to CS for the same period of time but without DFP treatment (Fig. 6c). Similarly, WT mice exposed to CS for 6 or 8 weeks and administered DFP after 4 weeks of CS exposure showed improved weight gain and had lower lung mitochondrial iron loading than mice that were exposed to CS for 6 or 8 weeks but that were not treated with DFP (Fig. 6d,e). WT mice with CS-induced pulmonary inflammation and injury (higher BAL leukocyte counts, higher total BALF protein levels, higher BALF IL-33 protein concentration and higher whole-lung tissue IL-6 protein concentration after 4 weeks of CS exposure) that were then treated with DFP during an additional 2 or 4 weeks of CS exposure also showed significant reductions in pulmonary inflammation (BAL total leukocyte counts, and BALF IL-33 and IL-6 protein concentrations) and acute lung injury (total BALF protein) after 2 and 4 weeks of DFP treatment versus mice exposed to CS for the same duration but not treated with DFP (Fig. 6f,g and Supplementary Fig. 10c–e).

DISCUSSION

GWAS have provided compelling associations for multiple susceptibility loci associated with COPD; most of these loci—including *IRP2* (15q25), family with sequence similarity 13, member A (*FAM13A*) and hedgehog-interacting protein (*HHIP*)—have been well replicated^{3,7,10,41–47}. Here we characterize, for the first time to our knowledge, the functional role of one of these genes, *IRP2* (*IREB2*), in the pathogenesis of COPD. Consistent with increased *IRP2* expression in human subjects with COPD⁴, we confirm that *Irp2* promotes COPD in two experimental mouse models of COPD.

By using novel experimental approaches and integrating unbiased *IRP2* target identification in cells and mouse lungs with human COPD expression data, we demonstrate that *IRP2* regulates mitochondria-related pathways in the lung. We validate this critical regulation in two well-established human COPD cohorts and show a strong association between the differential expression of mitochondrial genes and *IRP2* expression in subjects with COPD (Fig. 6h). Furthermore, we demonstrate that *Irp2* promotes mitochondrial dysfunction in experimental COPD (Fig. 6h), which may ultimately lead to epithelial cell death and emphysematous destruction associated with COPD¹. It is probably the case that cells in the lung that rely on mitochondrial function to promote cellular homeostasis may be affected by increased *IRP2* expression. These types of cells may include ciliated epithelial cells of

the respiratory tract, which rely on mitochondria for ATP generation for efficient ciliary-beat frequency, and parenchymal type II alveolar epithelial cells, which rely on their abundant stocks of mitochondria to regulate surfactant production. These data are consistent with earlier observations that increasing *IRP2* is detrimental to cells⁴⁸ and mice²¹ and that COPD itself is associated with mitochondrial dysfunction and altered mitochondrial dynamics^{17,49–51}. Further investigations into the valency of the accumulating mitochondrial non-heme iron (i.e., Fe²⁺ or Fe³⁺) and the role of *IRP2* in regulating mitochondrial heme biosynthesis will provide important additional insights needed to fully elucidate the role of *IRP2* in regulating mitochondrial function in the lung.

Our data showing that *IRP2* promotes mitochondrial iron overload in experimental COPD is consistent with previous observations that CS exposure increases iron deposition systemically and in alveolar macrophages from human subjects with COPD^{52,53}. Such iron deposition may also be consistent with recent reports of anemia being associated with poor clinical and functional outcomes in COPD^{54–56} and with reports that systemic inflammation in COPD upregulates serum hepcidin⁵⁷. Excess tissue or, more specifically, excess mitochondrial iron may generate hydroxyl radicals that promote inflammation, cell death and oxidative stress²¹, all of which contribute to the pathogenesis of COPD¹.

We hypothesize that as a consequence of sustained expression of *IRP2*, COX increases in airway epithelial cells and may become pathogenic, preceding and leading to mitochondrial dysfunction, epithelial cell damage, inflammation and emphysematous destruction in experimental COPD (Fig. 6h). In line with our observations, a recent study³⁶ reported that high COX activity is required for maximal airway responsiveness³⁶, and others have shown that COX activity is increased in skeletal muscle from human subjects with COPD⁵⁸. We also illustrate that COX may be a central determinant in the lung for the regulation of mitochondrial iron in response to CS exposure. Consistent with this notion, individuals with mutations in genes that encode subunits of COX have abnormal regulation of iron (sideroblastic anemia³⁵) and defects in mitochondrial heme biosynthesis⁵⁹.

Finally, we highlight the efficacy of therapeutically targeting mitochondrial iron in COPD. Specifically, redistributing excessive mitochondrial iron using the membrane-permeant iron chelator DFP alleviated experimental COPD. This cytoprotective effect of DFP is intriguing given the availability of DFP for human use in the treatment of beta-thalassemia⁴⁰ and in various clinical trials. DFP can shuttle iron not only out of mitochondria but also between other cellular organelles, such as nuclei and endosomes, to extracellular apotransferrin. DFP can also mobilize iron from iron-loaded cells and donate it to pre-erythroid cells for hemoglobin synthesis^{39,40}. Mitochondria-independent effects of DFP may therefore account for the synergistic effects of DFP with *Irp2* deficiency in our experimental COPD model.

Taken together, these studies provide valuable new insights into the mechanistic role of the COPD susceptibility gene *Irp2* in experimental COPD. Our results strongly suggest that *IRP2* is one of the potentially multiple COPD susceptibility genes located in the COPD-associated region of chromosome 15q25 identified by GWAS. Although GWAS generate clues to help us identify targets that play important functional roles in the pathogenesis of complex diseases such as COPD, improved integrative approaches for the identification of key genes and functional genetic variants in the GWAS-identified loci are needed. Recent analyses indicate that the *IRP2*-15q25 locus includes multiple genetic variants simultaneously associated with COPD and

the expression of nearby genes (COPD eQTLs (expression quantitative trait loci))⁶⁰; it is therefore possible that multiple genes located in close proximity to *IRP2* (for example, the nicotinic receptors cholinergic receptor, nicotinic, alpha 3 or *CHRNA3* and *CHRNA5*) may influence COPD susceptibility.

Genes, such as *IRP2*, that are involved in CS-induced stress responses, particularly those converging on the mitochondria, act as first responders in cellular and possibly systemic iron processing which, if sustained for long periods of time, may have deleterious effects at the molecular, cellular and tissue levels, leading to mitochondrial dysfunction and subsequent cell death and the initiation of inflammation that ultimately result in the development of COPD. Finally, our study strongly supports the use of mitochondrial-iron chelators as novel therapeutic approaches for COPD.

METHODS

Methods and any associated references are available in the [online version of the paper](#).

Accession codes. Gene Expression Omnibus: RIP-seq data are available under accession code [GSE57073](#), and microarray data for WT versus *Irp2*^{-/-} mice are available under accession code [GSE57048](#).

Note: Any Supplementary Information and Source Data files are available in the online version of the paper.

ACKNOWLEDGMENTS

The authors thank J.S. Moon, H.C. Lam, K. Taylor and B. Ding for technical assistance. The authors also acknowledge S. Chan (Harvard Medical School) for the cyto-GRX2 and mito-GRX2 plasmids, Y. Hua (Columbia University) for the breeding of the *Sco2*^{ki/ki} and *Sco2*^{ki/ko} mice and J. Connelly (ApoPharma Inc.) for providing Ferriprox. The authors also thank R. Rubio for assistance with RNA-seq, Y. Shao for assistance with the microarray study and M. Ericsson for assistance with transmission electron microscopy. The authors also acknowledge discussion and input from S.W. Rytter, C.A. MacRae and P.Y. Sips. This work was supported by US National Institutes of Health (NIH) grants P01-HL114501 (A.M.K.C.), R01-HL055330 (A.M.K.C.), R01-HL079904 (A.M.K.C.), R01-A1111475-01 (C.A.O.), R01-HL86814 (C.A.O.), R21-HL11835 (C.A.O.), HL122513 (H.P.), R01-HL086936 (to J.M.D'A.) and P01-HD080642 (Project 2 to E.A.S.), NIH-National Heart, Lung and Blood Institute grant K99-HL125899 (S.M.C.), American Lung Association Biomedical Research grant RG-348928 (S.M.C.), a Flight Attendants Medical Research Institute (FAMRI) clinical innovator award (A.M.K.C.), clinical innovator FAMRI grant CIA#123046 (C.A.O.), FAMRI Young Clinical Scientist awards YFEL141004 (F.P.) and YFEL103236 (M.P.G.), and US Department of Defense grant W911F-15-1-0169 (E.A.S.). S.M.C., A.M.K.C., J.Q. and E.K.S. were also supported by NIH grant P01-HL105339 (to E.K.S.). K.G. was supported by NIH grant R01-HL11759 (to J.Q., G.C.Y. and E.K.S.). C.A.O. was also supported by NIH grants R21-ES025379-01 (to A. Fedulov), P01-HL105339 (to E.K.S.) and P01-HL114501 (to A.M.K.C.) and by Brigham and Women's Hospital-Lovelace Respiratory Research Institute Research Consortium grants. G.M. and C.K. were supported by NIH grant R01-GM088999 (to G.M.). M.C.G. and T.A.R. acknowledge support from the intramural research program of the Eunice Kennedy Shriver National Institute of Child Health and Human Development, NIH. Additional support was provided by the Muscular Dystrophy Association (E.A.S.) and the J. Willard and Alice S. Marriott Foundation (E.A.S.).

AUTHOR CONTRIBUTIONS

S.M.C. and A.M.K.C. conceived and designed the study. S.M.C., K.G., M.E.L.-C., M.A.P., I.I.S., E.P., C.K., K.M., Z.-H.C., N.C.W., K.T.R., M.C.G. and A.M. performed experiments. K.G. analyzed RIP-seq, gene expression and human expression data and performed functional clustering analysis. A.R.B. and M.C. reconstructed and analyzed MCC images. S.C.M. provided technical support for the MCC experiments. C.A.O., F.P. and H.P. analyzed morphometric data. M.C.G. and T.A.R. provided the *Irp2*^{-/-} mice. E.A.S. provided the *Sco2*^{ki/ki} and *Sco2*^{ki/ko} mice, and M.P.G. and J.M.D'A. provided technical support. D.L.D. helped with the LGRC human data set. S.M.C., K.G., G.-C.Y., J.Q., E.K.S., G.M., C.A.O. and A.M.K.C. provided critical analysis and discussions. S.M.C. and A.M.K.C. wrote the paper with significant input and contributions from K.G. and C.A.O. All coauthors reviewed and approved the final manuscript.

COMPETING FINANCIAL INTERESTS

The authors declare competing financial interests: details are available in the [online version of the paper](#).

Reprints and permissions information is available online at <http://www.nature.com/reprints/index.html>.

- Barnes, P.J., Shapiro, S.D. & Pauwels, R.A. Chronic obstructive pulmonary disease: molecular and cellular mechanisms. *Eur. Respir. J.* **22**, 672–688 (2003).
- Hogg, J.C. *et al.* The nature of small-airway obstruction in chronic obstructive pulmonary disease. *N. Engl. J. Med.* **350**, 2645–2653 (2004).
- Siedlinski, M. *et al.* Dissecting direct and indirect genetic effects on chronic obstructive pulmonary disease (COPD) susceptibility. *Hum. Genet.* **132**, 431–441 (2013).
- DeMeo, D.L. *et al.* Integration of genomic and genetic approaches implicates *IREB2* as a COPD susceptibility gene. *Am. J. Hum. Genet.* **85**, 493–502 (2009).
- Qiu, W. *et al.* ECLIPSE Investigators. Genetics of sputum gene expression in chronic obstructive pulmonary disease. *PLoS One* **6**, e24395 (2011).
- Hardin, M. *et al.* *CHRNA3/5*, *IREB2* and *ADCY2* are associated with severe chronic obstructive pulmonary disease in Poland. *Am. J. Respir. Cell Mol. Biol.* **47**, 203–208 (2012).
- Pillai, S.G. *et al.* ICGN Investigators. A genome-wide association study in chronic obstructive pulmonary disease (COPD): identification of two major susceptibility loci. *PLoS Genet.* **5**, e1000421 (2009).
- Saccone, N.L. *et al.* Multiple independent loci at chromosome 15q25.1 affect smoking quantity: a meta-analysis and comparison with lung cancer and COPD. *PLoS Genet.* **6**, e1001053 (2010).
- Thorgeirsson, T.E. *et al.* A variant associated with nicotine dependence, lung cancer and peripheral arterial disease. *Nature* **452**, 638–642 (2008).
- Lee, J.H. *et al.* *IREB2* and *GALC* are associated with pulmonary artery enlargement in chronic obstructive pulmonary disease. *Am. J. Respir. Cell Mol. Biol.* **52**, 365–376 (2015).
- Meyron-Holtz, E.G. *et al.* Genetic ablations of iron-regulatory proteins 1 and 2 reveal why iron-regulatory protein 2 dominates iron homeostasis. *EMBO J.* **23**, 386–395 (2004).
- Ghosh, M.C. *et al.* Deletion of iron-regulatory protein 1 causes polycythemia and pulmonary hypertension in mice through translational derepression of *HIF2α*. *Cell Metab.* **17**, 271–281 (2013).
- LaVaute, T. *et al.* Targeted deletion of the gene encoding iron-regulatory protein 2 causes misregulation of iron metabolism and neurodegenerative disease in mice. *Nat. Genet.* **27**, 209–214 (2001).
- Jeong, S.Y. *et al.* Iron insufficiency compromises motor neurons and their mitochondrial function in *Irp2*-null mice. *PLoS One* **6**, e25404 (2011).
- Cooperman, S.S. *et al.* Microcytic anemia, erythropoietic protoporphyria and neurodegeneration in mice with targeted deletion of iron-regulatory protein 2. *Blood* **106**, 1084–1091 (2005).
- Yoshida, T. *et al.* Rtp801, a suppressor of mTOR signaling, is an essential mediator of cigarette smoke-induced pulmonary injury and emphysema. *Nat. Med.* **16**, 767–773 (2010).
- Mizumura, K. *et al.* Mitophagy-dependent necroptosis contributes to the pathogenesis of COPD. *J. Clin. Invest.* **124**, 3987–4003 (2014).
- Lam, H.C. *et al.* Histone deacetylase 6-mediated selective autophagy regulates COPD-associated cilia dysfunction. *J. Clin. Invest.* **123**, 5212–5230 (2013).
- Leopold, P.L. *et al.* Smoking is associated with shortened airway cilia. *PLoS One* **4**, e8157 (2009).
- Thorley, A.J. & Tetley, T.D. Pulmonary epithelium, cigarette smoke and chronic obstructive pulmonary disease. *Int. J. Chron. Obstruct. Pulmon. Dis.* **2**, 409–428 (2007).
- Moroishi, T., Nishiyama, M., Takeda, Y., Iwai, K. & Nakayama, K.I. The FBXL5-IRP2 axis is integral to control of iron metabolism *in vivo*. *Cell Metab.* **14**, 339–351 (2011).
- An, C.H. *et al.* *TLR4* deficiency promotes autophagy during cigarette smoke-induced pulmonary emphysema. *Am. J. Physiol. Lung Cell. Mol. Physiol.* **303**, L748–L757 (2012).
- Braber, S. *et al.* Cigarette smoke-induced lung emphysema in mice is associated with prolyl endopeptidase, an enzyme involved in collagen breakdown. *Am. J. Physiol. Lung Cell. Mol. Physiol.* **300**, L255–L265 (2011).
- Kantrow, S.P., Shen, Z., Jagneaux, T., Zhang, P. & Nelson, S. Neutrophil-mediated lung permeability and host defense proteins. *Am. J. Physiol. Lung Cell. Mol. Physiol.* **297**, L738–L745 (2009).
- Qiu, C. *et al.* Anti-interleukin-33 inhibits cigarette smoke-induced lung inflammation in mice. *Immunology* **138**, 76–82 (2013).
- Hubeau, C., Kubera, J.E., Masek-Hammerman, K. & Williams, C.M. Interleukin-6 neutralization alleviates pulmonary inflammation in mice exposed to cigarette smoke and poly(I:C). *Clin. Sci.* **125**, 483–493 (2013).
- Galy, B. *et al.* Iron-regulatory proteins secure mitochondrial iron sufficiency and function. *Cell Metab.* **12**, 194–201 (2010).
- Fujimura, M., Morita-Fujimura, Y., Murakami, K., Kawase, M. & Chan, P.H. Cytosolic redistribution of cytochrome c after transient focal cerebral ischemia in rats. *J. Cereb. Blood Flow Metab.* **18**, 1239–1247 (1998).
- Huang, M.L. *et al.* Elucidation of the mechanism of mitochondrial iron loading in Friedreich's ataxia by analysis of a mouse mutant. *Proc. Natl. Acad. Sci. USA* **106**, 16381–16386 (2009).

30. Hentze, M.W., Muckenthaler, M.U., Galy, B. & Camaschella, C. Two to tango: regulation of mammalian iron metabolism. *Cell* **142**, 24–38 (2010).
31. Shaw, G.C. *et al.* Mitoferrin is essential for erythroid iron assimilation. *Nature* **440**, 96–100 (2006).
32. Whitnall, M. *et al.* Identification of nonferritin mitochondrial iron deposits in a mouse model of Friedreich's ataxia. *Proc. Natl. Acad. Sci. USA* **109**, 20590–20595 (2012).
33. Slebos, D.J. *et al.* Mitochondrial localization and function of heme oxygenase-1 in cigarette smoke-induced cell death. *Am. J. Respir. Cell Mol. Biol.* **36**, 409–417 (2007).
34. Clemente, P. *et al.* hCOA3 stabilizes cytochrome c oxidase 1 (COX1) and promotes cytochrome c oxidase assembly in human mitochondria. *J. Biol. Chem.* **288**, 8321–8331 (2013).
35. Gattermann, N. *et al.* Heteroplasmic point mutations of mitochondrial DNA affecting subunit I of cytochrome c oxidase in two patients with acquired idiopathic sideroblastic anemia. *Blood* **90**, 4961–4972 (1997).
36. Huttemann, M. *et al.* Cytochrome c oxidase subunit 4 isoform 2–knockout mice show reduced enzyme activity, airway hyporeactivity and lung pathology. *FASEB J.* **26**, 3916–3930 (2012).
37. Yang, H. *et al.* Analysis of mouse models of cytochrome c oxidase deficiency owing to mutations in *Sco2*. *Hum. Mol. Genet.* **19**, 170–180 (2010).
38. Ning, W. *et al.* Comprehensive gene expression profiles reveal pathways related to the pathogenesis of chronic obstructive pulmonary disease. *Proc. Natl. Acad. Sci. USA* **101**, 14895–14900 (2004).
39. Sohn, Y.S., Breuer, W., Munnich, A. & Cabantchik, Z.I. Redistribution of accumulated cell iron: a modality of chelation with therapeutic implications. *Blood* **111**, 1690–1699 (2008).
40. Filosa, A. *et al.* Long-term treatment with deferiprone enhances left ventricular ejection function when compared to deferoxamine in patients with thalassemia major. *Blood Cells Mol. Dis.* **51**, 85–88 (2013).
41. Hancock, D.B. *et al.* Meta-analyses of genome-wide association studies identify multiple loci associated with pulmonary function. *Nat. Genet.* **42**, 45–52 (2010).
42. Repapi, E. *et al.* Genome-wide association study identifies five loci associated with lung function. *Nat. Genet.* **42**, 36–44 (2010).
43. Lambrechts, D. *et al.* The 15q24/25 susceptibility variant for lung cancer and chronic obstructive pulmonary disease is associated with emphysema. *Am. J. Respir. Crit. Care Med.* **181**, 486–493 (2010).
44. Cho, M.H. *et al.* A genome-wide association study of COPD identifies a susceptibility locus on chromosome 19q13. *Hum. Mol. Genet.* **21**, 947–957 (2012).
45. Cho, M.H. *et al.* Risk loci for chronic obstructive pulmonary disease: a genome-wide association study and meta-analysis. *Lancet Respir. Med.* **2**, 214–225 (2014).
46. Cho, M.H. *et al.* Variants in *FAM13A* are associated with chronic obstructive pulmonary disease. *Nat. Genet.* **42**, 200–202 (2010).
47. Wilk, J.B. *et al.* A genome-wide association study of pulmonary function measures in the Framingham Heart Study. *PLoS Genet.* **5**, e1000429 (2009).
48. Rensvold, J.W. *et al.* Complementary RNA and protein profiling identifies iron as a key regulator of mitochondrial biogenesis. *Cell Reports* **3**, 237–245 (2013).
49. Agarwal, A.R., Yin, F. & Cadenas, E. Short-term cigarette smoke exposure leads to metabolic alterations in lung alveolar cells. *Am. J. Respir. Cell Mol. Biol.* **51**, 284–293 (2014).
50. Caron, M.A., Debigaré, R., Dekhuijzen, P.N. & Maltais, F. Comparative assessment of the quadriceps and the diaphragm in patients with COPD. *J. Appl. Physiol.* **107**, 952–961 (2009).
51. Crul, T. *et al.* Gene expression profiling in vastus lateralis muscle during an acute exacerbation of COPD. *Cell. Physiol. Biochem.* **25**, 491–500 (2010).
52. Ghio, A.J. *et al.* Particulate matter in cigarette smoke alters iron homeostasis to produce a biological effect. *Am. J. Respir. Crit. Care Med.* **178**, 1130–1138 (2008).
53. Philippot, Q. *et al.* Increased iron sequestration in alveolar macrophages in chronic obstructive pulmonary disease. *PLoS One* **9**, e96285 (2014).
54. Silverberg, D.S. *et al.* Anemia and iron deficiency in COPD patients: prevalence and the effects of correction of the anemia with erythropoiesis stimulating agents and intravenous iron. *BMC Pulm. Med.* **14**, 24 (2014).
55. Schneckenpointner, R. *et al.* The clinical significance of anemia and disturbed iron homeostasis in chronic respiratory failure. *Int. J. Clin. Pract.* **68**, 130–138 (2014).
56. Nickol, A.H. & Frise, M.C. A cross-sectional study of the prevalence and associations of iron deficiency in a cohort of patients with chronic obstructive pulmonary disease. *BMJ Open* **5**, e007911 (2015).
57. Tandara, L. *et al.* Systemic inflammation upregulates serum hepcidin in exacerbations and stable chronic obstructive pulmonary disease. *Clin. Biochem.* **48**, 1252–1257 (2015).
58. Sauleda, J. *et al.* Cytochrome oxidase activity and mitochondrial gene expression in skeletal muscle of patients with chronic obstructive pulmonary disease. *Am. J. Respir. Crit. Care Med.* **157**, 1413–1417 (1998).
59. Antonicka, H. *et al.* Mutations in *COX10* result in a defect in mitochondrial heme A biosynthesis and account for multiple, early-onset clinical phenotypes associated with isolated COX deficiency. *Hum. Mol. Genet.* **12**, 2693–2702 (2003).
60. Castaldi, P.J. *et al.* Genetic control of gene expression at novel and established chronic obstructive pulmonary disease loci. *Hum. Mol. Genet.* **24**, 1200–1210 (2015).

ONLINE METHODS

Animals. *Irp2*^{-/-} and WT littermate control mice were from a mixed genetic background consisting of 129S4/SvJae and C57BL/6 and were from T. Rouault (National Institute of Child Health and Human Development). *Sco2*^{ki/ki} (C57BL/6), *Sco2*^{ki/ko} (C57BL/6) and WT (C57BL/6) littermate mice were from E. Schon (Columbia University). *Sco2*^{ki/ki} mice have a *Sco2* knock-in (KI) mutation on both alleles, and *Sco2*^{ki/ko} mice have a *Sco2* knock-in (KI) mutation on one allele and have *Sco2* deleted on the other allele (KO)³⁷. Wild-type (C57BL/6) and *Fxn*^{ki/ko} (C57BL/6) mice were purchased from the Jackson Laboratory. *Fxn*^{ki/ko} mice harbor one allele of the frataxin (GAA) 230Δneo expansion mutation (*Fxn*^{tm1.1Pand}) on one chromosome, and one allele of the frataxin exon 4–deleted mutation (*Fxn*^{tm1Mkn}) on the homologous chromosome. All animals were housed in the same room and kept under a 12-h light and dark cycle. The iron content of the standard diet was 200 mg per kg body weight (mg/kg). Power was not explicitly calculated for each experiment. Numbers of mice were typically chosen based on prior experiments. Cages were chosen at random for CS or RA exposures. We did not use a blinded approach during the CS exposure, as mice needed to be monitored during and after smoke exposure. In addition, mouse cages exposed to CS displayed a distinctive smell and color, and were obvious to the investigators. All animal experimental protocols were approved by the Harvard Standing Committee for Animal Welfare and by the Institutional Animal Care and Use Committees of Brigham and Women's Hospital.

In vivo CS exposures, chemical treatments and diet modifications. We selected age- and sex-matched mice, starting at 6–12 weeks of age, at random and exposed them to total body CS in a stainless steel chamber using a whole-body smoke exposure device (Model TE-10, Teague Enterprises) for 2 h per day, 5 d per week for 4 weeks or 4–6 months. Age-matched male and female mice were used for all CS exposures. Mice were exposed to CS (mainstream and sidestream smoke) from 100 3R4F cigarettes (University of Kentucky), which correlated to an average total particulate matter (TPM) of 150 mg/m³. For animals subjected to cigarette smoke exposure, early death was used as an exclusion criterion. At the end of the exposure regimen, we euthanized mice by CO₂ narcosis, cannulated the tracheas and inflated the lungs with PBS at 25 cm of H₂O pressure. We tied off the left lung with a suture, dissected it and place it into liquid nitrogen. We fixed the right lung in 4% formalin at 4 °C overnight. A proximal portion of the left lung (4-month exposures only) was fixed for transmission electron microscopy (TEM) analysis.

Mice exposed to CS for 4 weeks had modifications to their dietary iron as follows: diet 1 (control diet) from Harlan Laboratories (TD.94045 AIN-93G), which contained 300 parts per million (p.p.m.) iron. Diet 2 (iron-deficient diet) from Harlan Laboratories (TD.10210), which contained 2–6 p.p.m. iron. Diet 3 (iron-replete diet) from Harlan Laboratories (TD.10213), which contained 2% carbonyl iron. Iron diets were exchanged for normal diets upon weaning at 3 weeks of age and used throughout the smoke exposures. We weighed each animal on a weekly basis, and we recorded the quantity of chow consumed, comparing it to that for mice on a normal-iron diet. We administered deferiprone or Ferriprox solution (1 mg/ml) (ApoPharma Inc.) prophylactically in the animals' drinking water for the duration of the smoke exposure. We also administered deferiprone therapeutically in the animals' drinking water, initiating therapy after 4 weeks of smoke exposure and continuing therapy for an additional 2–4 weeks. Animals were checked daily, and the quantity of water consumed was compared to that for control mice. Water solutions were changed twice weekly.

Hyperoxia exposures. We exposed age- and sex-matched *Irp2*^{-/-} and WT littermate mice (129S4/SvJae and C57BL/6 background), starting at 10 weeks of age and selected at random, to hyperoxia (>99% O₂) at a flow rate of 12 liters/min in a 3.70-ft³ Plexiglas exposure chamber⁶¹, with access to chow and water *ad libitum*. We assessed survival by checking the mice at regular intervals over 0–120 h.

Cecal ligation-puncture (CLP) sepsis model. CLP was done as described⁶². Briefly, under aseptic conditions, we incised the abdominal skin and dissected the abdominal muscles of age- and sex-matched *Irp2*^{-/-} and WT littermate mice (129S4/SvJae and C57BL/6 background), starting at 10 weeks of age and selected

at random, to gain access to the peritoneal cavity. We located the mouse cecum and we ligated 75% of it with a 6-0 silk suture and perforated it with a 21 G needle by one through-and-through puncture (two holes) near to the area of ligation. Sham-operated mice underwent the same procedure without ligation and puncture of the exposed cecum. After surgery, we intraperitoneally (i.p.) injected 1 ml of prewarmed (37 °C) normal saline to restore heat and hydration of the operated mice.

Electrophoretic mobility shift assay (EMSA). *Irp2* EMSAs were carried out using the LightShift Chemiluminescent RNA EMSA Kit (Thermo Scientific) with a biotinylated IRE, according to the manufacturer's instructions. Supershift assays were carried out using 2.5 μg of anti-*Irp2* IgG (NB100-1798, Novus Biologicals).

Immunohistochemistry and immunofluorescence staining. We prepared and stained formalin-fixed, paraffin-embedded 5-μm-thick lung sections using standard procedures. Briefly, sections were deparaffinized through graded alcohols and washed in PBS. Heat-activated antigen retrieval was performed in a microwave oven using a citrate buffer (Target Retrieval Solution, S1699, DAKO) for 10 min. Endogenous peroxidases were blocked using a peroxidase blocker (DAKO Cytomation), and the slides were blocked for nonspecific protein binding by incubating in 10% normal serum for 45 min. Tissues were immunostained with a rabbit primary IgG to *Irp2* (LS-B48, LS Bio) at a 1:50 dilution, with mouse anti-cytochrome c, (556433, BD Biosciences) at a 1:250 dilution, with rabbit monoclonal IgG to cytochrome c EPR1327 (D00355 Abcam) at a 1:50 dilution, or with rabbit anti-LC3B (L7543, Sigma-Aldrich) at a 1:400 dilution and signals were developed using the VECTASTAIN Elite ABC Kit (PK-6101; Vector Laboratories), according to the manufacturer's protocol. Hematoxylin and eosin stains were purchased from Sigma-Aldrich, and staining was carried out as per the manufacturer's instructions. The negative control consisted of substituting PBS for the primary antibody.

Epifluorescence microscopy. Briefly, tissues were stained with goat polyclonal IgG to *Irp2* (ab106926, Abcam) at a 1:50 dilution or with rabbit monoclonal IgG to *Irp2* (ab181153, Abcam) at a 1:50 dilution. Co-staining for type II epithelial cells was carried out using a rabbit polyclonal IgG to prosurfactant protein C (Pro-SPC) (ab90716, Abcam) at a 1:50 dilution and for type I epithelial cells using anti-mouse podoplanin Alexa Fluor 488–conjugated IgG (53-5381-80, Affymetrix) at a 1:500 dilution. Co-staining for *Irp2* and markers of ciliated airway epithelial cells was conducted using a rabbit IgG for acetyl- α -tubulin (Lys40) (D20G3, Cell Signaling Technology) at a 1:50 dilution, and co staining for non-ciliated secretory epithelial cells was conducted using a rabbit polyclonal IgG to uteroglobin (ab40873, Abcam) at a 1:100 dilution. Secondary staining was carried out using goat anti-rabbit IgG (H + L) rhodamine red conjugate (R-6394, Life Technologies) at a 1:500 dilution or donkey anti-goat IgG (H + L) secondary antibody–Alexa Fluor 488 conjugate (A-11055, Life technologies) at a 1:500 dilution. Nuclei were counter-stained using TO-PRO-3 Iodide (T3605, Life Technologies) at a 1:1,000 dilution or Hoechst (33342, ThermoFisher Scientific) at a 1:300 dilution.

Morphometric analysis of lung sections. Formalin-fixed lung samples were cut parasagittally and embedded in paraffin. We performed Modified Gill's staining as described previously⁶³. We quantified air-space enlargement using the mean linear intercept (chord)-length (MLI or L_m) method⁶³ or using a previously published, automated image-processing algorithm that calculates the area-weighted mean diameter or D_2 index⁶⁴. Briefly, randomized images were acquired (Axiophot; Carl Zeiss MicroImaging equipped with a digital camera Axiocam HR; Carl Zeiss MicroImaging) as black and white TIFF files using a microscope, a 20 \times objective, and a camera and software that can acquire high-quality digital images. 20–30 images (200 \times magnification) were captured per mouse in a randomized manner, with the observer blinded to the experimental condition, avoiding under-inflated areas of the lung (at 20 \times magnification). Lung sections were blinded by taping the slide identifiers before acquiring images and before data analysis. Random-number generations using excel and a gridded coverslip were used to choose the sample image area for acquisition in all cases.

Mean-chord-length measurements. This protocol measures mean alveolar chord length and alveolar area on paraffin-embedded lung sections stained with Gill's stain. Morphometry software converts images of lung sections to binary images (in which tissue is white and airspace is black), and then superimposes a uniform grid of horizontal and vertical lines (chords), and the software then quantifies the length of each chord within areas identified by the software as airspace⁶⁵. Using this method, it is possible to measure the size of the alveoli in all parts of the lung in a standardized and relatively automated manner⁶⁵. Airspace enlargement was quantified using the MLI method using Scion Image and customized macros to analyze airspace enlargement⁶⁵. Large airways, blood vessels, and other non-alveolar structures were manually removed from the images. The alveolar-chord-length macro was adapted from the macro available in NIH Image. Alveolar chord length for each image was calculated and the average mean chord length \pm s.e.m. for each mouse was calculated.

Measurement of alveolar diameters. This protocol measures the area-weighted mean diameter or D_2 index. Compared to the Lm , the D_2 index characterizes the heterogeneity in airspace sizes and has been used in the past to quantify airspace enlargement in many studies^{66–70}, where it has a higher sensitivity and specificity for discerning airspace enlargement in smoke-exposed mice⁶⁶. In this study, the D_2 index was calculated on paraffin-embedded lung sections stained with Gill's stain with randomized image acquisition as described above. The histological images were first thresholded to create a black-and-white image where white pixels correspond to air and black pixels correspond to tissue. To avoid errors associated with non-uniform illumination, each image was split into non-overlapping blocks, and the threshold for each block was calculated using the Otsu's method, which calculates the optimum threshold to minimize the intra-class variance of the black and white pixels⁷¹. The black-and-white images were then used to calculate a signed distance function where each pixel is assigned the negative of the distance to the nearest black (tissue) pixel. The resulting distance function had a deep minima near the center of each alveolar section and also many shallow local minima close to the alveolar walls created by small local fluctuations in the curvature of the alveolar walls. The shallow minima were removed by a morphological operator called the H minima transform⁷². The resulting modified distance map was then segmented using the watershed algorithm⁷³ into distinct regions, with each region corresponding to a section of an alveolus. The area occupied by each alveolar section was measured by counting the number of pixels in each region. The measured area was then converted to real units (O (μm^2) for mouse alveolar sections) by multiplying with a scaling factor. The area of each alveolar section A was then converted to an equivalent alveolar diameter, d as $d = 2\sqrt{A/\pi}$. From the measured equivalent diameters the area-weighted mean diameter D_2 as $D_2 = \frac{d^3}{d^2}$ was calculated.

Small-airway remodeling. We used a modification of a published morphometry method^{65,74} to quantify small-airway remodeling in formalin-fixed lung sections from WT and *Irp2*^{-/-} mice exposed to RA or CS for 6 months. Briefly, lung sections were stained with Masson's Trichrome stain (Sigma-Aldrich), and images were acquired using a light microscope (Axiophot; Carl Zeiss MicroImaging) equipped with a digital camera (Axiocam HRC; Carl Zeiss MicroImaging) at 200 \times magnification by a blinded, experienced reader as previously described⁶⁵. MetaMorph software (Molecular Device LLC) was used to measure the mean airway luminal diameter and the thickness of the sub-epithelial fibrosis layer stained blue by Masson's Trichrome stain at 12 separate sites around the airway by a different blinded, experienced reader. The mean (\pm s.e.m.) thickness of the sub-epithelial layer in microns was calculated for airways having a mean internal diameter between 300 and 699 μm . Sections of airways sharing their adventitia with arteries or other airways were not included in the analysis.

BALF isolation, cell counts and ELISA. Mice were euthanized by CO₂ narcosis, the tracheas cannulated and the lungs lavaged with 0.5-ml increments of ice-cold PBS eight times (4 ml total). BALF was centrifuged at 500g for 5 min. 1 ml red blood cell lysis buffer (Sigma-Aldrich) was added to the cell pellet and left on ice for 15 min followed by centrifugation at 600g for 3 min. The cell pellet was resuspended in 500 μl PBS, and leukocytes were counted using a hemocytometer. Specifically, 20 μl was removed for cell counting (performed in triplicate)

using a hemocytometer, and 80 μl was removed for cytocentrifuge preparations (Shandon Cytospin3, 300 r.p.m. for 5 min) and stained using the Hema3 staining system (Fisher Scientific). The percentages of macrophages, lymphocytes and polymorphonuclear leukocytes (PMNs) were counted in a total of 300 cells, and absolute numbers of each leukocyte subset were calculated.

Commercial ELISAs were used to measure the following analytes in duplicate in homogenates or BALF of lung samples from mice following the manufacturer's instructions: MMP-9 (Mouse Total MMP-9 DuoSet, DY6718, R&D Systems), cleaved caspase-3 (Human/Mouse Cleaved Caspase-3 (Asp175) DuoSet IC, R&D Systems DYC835-2), IL-6 (mouse IL-6 DuoSet, R&D Systems DY406), IL-33 (mouse IL-33 DuoSet, R&D Systems DY3626-05), IL-18 (IL-18/IL1F4 ELISA kit 7625, R&D Systems) and IL-1 β (Mouse IL-1 β /IL-1F2 R&D Systems DY401-05).

Assessment of mucociliary clearance. Mucociliary clearance was quantified using a non-invasive, oropharyngeal aspiration procedure described previously¹⁸. Briefly, we anesthetized mice and introduced 50 μl of normal saline containing approximately 0.3–0.5 mCi of ^{99m}Tc-technetium sulfur colloid (^{99m}Tc-sc) (Brigham and Women's Hospital) into the distal part of the oropharynx by aspiration. We immediately imaged mouse lungs after aspiration ($t = 0$ h) and at 1 h and 3 h. Whole-mouse three dimensional (3D) micro single-photon emission computed tomography (μ -SPECT) images from 10-min acquisitions at 0-, 1-, and 3-h time points were obtained, reconstructed, blindly analyzed and expressed as the percentage removed by mucociliary clearance. Regional lung deposition of ^{99m}Tc-sc, characterized by calculating the central (area closest to the trachea) to peripheral airway distributions ratio (C:P ratio), was corrected for, as described previously⁷⁵. To correct for any abnormality in distribution, MCC rates were corrected for C:P differences using standard multi-variable linear regression⁷⁶.

RIP-seq. Three 15-cm² dishes (1.5×10^6 cells) of Beas2B cells (purchased from ATCC), treated with or without 10 μM DFO (16 h), were washed with ice-cold PBS and collected into 2-ml microcentrifuge tubes by scraping. We carried out RNA immunoprecipitation using the Magna RIP RNA-Binding Protein Immunoprecipitation Kit (Millipore). 4 μg of mouse Irp2 IgG (7H6: sc-33682, Santa Cruz) or 4 μg of IgG mouse control antibody (sc-2749, Santa Cruz) were added to supernatants and incubated overnight at 4 $^\circ\text{C}$. We extracted RNA from Magna RIP beads by Trizol extraction. Samples ($n = 2$ biological replicates) were prepared for RNA-seq using the TruSeq RNA-seq Lib Prep Reagent (Illumina), and sequencing was performed on the Illumina HiSeq2000 platform. Sample preparation and sequencing was carried out by The Center for Cancer Computational Biology, Dana-Farber Cancer Institute, Boston, MA (<http://cccb.dfci.harvard.edu>). RIP-seq data (GEO accession number GSE57073) was analyzed as follows. Sequenced reads for two biological replicates each in control (Ctl) and DFO samples, as well as Ctl-IgG and DFO-IgG, were aligned to the human hg19 known transcriptome using bowtie2-2.0.6 and tophat-2.0.7.Linux_x84_64. Any unmapped reads were then allowed to map to the hg19 genome. Aligned reads were then combined from replicates and the HOMER algorithm (<http://homer.salk.edu/homer/ngs/index.html>) was used to identify and annotate 'peaks', or regions enriched for reads in one sample compared to another. Peak-calling was performed on the aligned reads, resulting in the identification of 3,497 'common' peaks (mapping to 1,806 genes) that were shared between the control (Ctl) and DFO samples as well as Ctl-specific peaks and DFO-specific peaks. Validation of our data included the detection of peaks in known IRP2 targets, including ferritin and TfR (**Supplementary Fig. 4e,f**). We also estimated the percentage of peaks with the known IRE-binding motif (CAGWGH)⁷⁷.

Four primary comparisons were made: Ctl compared to Ctl-IgG (Ctl/IgG), DFO compared to DFO-IgG (DFO/IgG), Ctl compared to DFO (Ctl/DFO) and DFO compared to Ctl (DFO/Ctl). The first two comparisons identified where IRP2 is bound in either Ctl or DFO samples, whereas the latter two comparisons highlight where IRP2 is uniquely bound in only the Ctl or DFO sample (**Supplementary Fig. 4d**). In each comparison a peak was associated with a genomic region if that peak had a twofold enrichment of the tag relative to the input sample, a Poisson $P < 0.1$ and a peak-score (position-adjusted read counts) greater than 5.



To build a robust set of peaks for further analysis, we identified peaks common between the different comparisons using HOMER's 'mergePeaks' function. 3,497 common peaks (where IRP2 is bound in both Ctl and DFO) were identified as shared between the Ctl/IgG and DFO/IgG comparisons. Ctl-specific peaks and DFO-specific peaks were identified by determining peaks common to the Ctl/IgG and Ctl/DFO or the DFO/IgG and DFO/Ctl comparisons, respectively (Supplementary Fig. 4d). For peaks belonging to one of these three sets, we used HOMER's 'annotatePeaks' function to scan the genomic sequence of the peak regions for the known IRE-binding motif (CAGWGH)⁷⁷ and to map peaks to their target genes. Common peaks mapped to 1,806 unique gene transcripts and Ctl-specific and DFO-specific peaks mapped to 2,203 and 2,135 unique gene transcripts, respectively (Supplementary Fig. 4d).

Gene expression microarray analysis. The GeneChip Mouse Gene 1.0 ST Array (Affymetrix) was used to assess gene expression in the *Irp2*^{-/-} and WT mice. RNA was isolated from lungs harvested from WT age-matched ($n = 3$ males and 3 females) and *Irp2*^{-/-} ($n = 3$ males and 3 females) using the RNeasy Mini Kit (Qiagen). The gene expression data GEO accession number GSE57048 was analyzed as follows. GSE57048 was robust multiarray average (RMA)-normalized, and probe sets were mapped to EntrezGene IDs using a custom Chip Definition Files (CDF)⁷⁸. To compare the expression data to the RIP-seq data, we selected 16,573 genes on the expression array that belong to a single conserved homologous group (<http://www.ncbi.nlm.nih.gov/homologene/>) with the corresponding human homolog identified. For these genes the expression difference between the *Irp2*^{-/-} and WT mice was quantified using an unpaired two-tailed *t*-test.

Functional enrichment clustering analysis. To evaluate how IRP2 may affect the activity of cellular pathways in the lung, we carried out functional enrichment analysis using the Database for Annotation, Visualization, and Integrated Discovery (DAVID)⁷⁹ tool^{79,80}. DAVID analysis (<http://david.abcc.ncifcrf.gov>) was carried out on the genes in each of three RIP-seq-defined sets (Ctl, DFO and common), both independently and combined. To better interpret the results of this analysis, the fast-greedy community-structure algorithm⁸¹ was applied to a network defined by the GO annotations between the genes identified in the RIP-seq analysis and the GO terms identified as enriched (false-discovery rate (FDR) $< 1 \times 10^{-3}$) in the DAVID analysis on the combined gene set. This network analysis resulted in the identification of five communities containing related sets of genes and terms (Supplementary Fig. 4g). For each community identified in the RIP-seq data, the values of the *t*-statistic for genes in the community was compared to those not in the community, and a 'meta' *t*-statistic and associated *P* value was computed, representing the significance of the association of the *Irp2*^{-/-} versus WT differentially expressed genes with genes in each of the RIP-seq communities⁸² (Fig. 2b). This analysis revealed a strong association between differentially expressed genes and genes in community 2.

Next we selected the genes belonging to community 2 that are also strongly differentially expressed ($P < 0.01$) in *Irp2*^{-/-} mice, as compared to WT mice. We examined to which GO categories (Gene Ontology terms⁸³) these genes are annotated and made three heat maps (Fig. 3a and Supplementary Fig. 5) based on whether they are annotated to mitochondrial functions (Fig. 3a), protein localization functions (Supplementary Fig. 5a) or other functions that belong to community 2 (Supplementary Fig. 5b). In each heat map, the rows were *z*-score-normalized to aid in visualizing differences in expression values.

Because RIP-seq was based on a specific IRP2 antibody that immunoprecipitated IRP2-mRNA complexes only (subtracting IgG-mRNA complexes as background) and then was followed by a comparison to the baseline gene expression in WT versus *Irp2*^{-/-} lungs, the effects of DFO are therefore not confounded on the functional enrichment clustering analysis carried out in this study, and the results are related to IRP2 only. Specifically, 83% (34 of 41) of the genes we show in Figure 3a were identified as a target of IRP2 in the Ctl versus IgG comparison (so they were in the common peaks, the CTRL-only peaks, or both). Only seven genes were identified in the DFO-only peak set.

Circos plot generation. By using the DAVID output from the combined gene-set analysis, a Circos plot was generated to graphically demonstrate the gene transcripts and pathways enriched and/or altered in our Ctl-specific (blue), DFO-specific (red) and common (purple) data sets. The inner ring of the Circos

plot is colored to represent the five identified functional communities. Because each gene belongs to only one community, genes were assigned to segments of the circle located within their community. Other genomic information associated with these genes, such as COPD differential expression and RIP-seq peak scores, was then visualized on different 'rings' aligned over these genes.

LGRC gene expression (mRNA) Circos plots. To identify any common pathways that may be dysregulated by IRP2 in subjects with COPD, we included gene expression data (mRNA) (Fig. 2a) from lung tissue of individuals with COPD and those from controls from the Lung Genomics Research Consortium (LGRC; <http://www.lung-genomics.org>) on the Circos plot. The Lung Genomics Research Consortium used lung tissue samples from the Lung Tissue Research Consortium and was funded by the National Heart, Lung, and Blood Institute. Lung tissue mRNA expression data was downloaded from the publicly available LGRC data set GSE47460. This 159-mRNA gene expression data set contained data from $n = 121$ individuals with COPD, $n = 20$ non-smokers and $n = 18$ smokers. We calculated the fold-change difference between the expression values for each gene in the COPD versus control samples; the inner ring (black ring) of the Circos plot shows the fold change for genes containing an identified IRP2 peak. Genes with fold changes of more than 1.5 or less than 1/1.5 were highlighted (green denotes lower than COPD, magenta denotes higher in COPD). Circos-plot generation allowed for the visualization of similarities and differences between the Ctl (blue), DFO (red) and common (purple) RIP-seq peak sets and human COPD RNA-seq (black).

Phenotypic characterization of emphysema and source of tissue. The LGRC provides genetic, molecular, and quantitative phenotype data as well as exclusion criteria, for human subjects in the NHLBI's Lung Tissue Research Consortium (LTRC) biorepository (<http://www.lung-genomics.org>). Lung tissue samples were collected as part of the routine care of patients and submitted with a standardized series of questions. In addition to standard spirometry, DLCO (diffusing capacity of the lungs for carbon monoxide) data were available. For controls, we included only individuals with a DLCO greater than 80%, and for test cases the DLCO was less than 80%.

As previously mentioned, the LGRC mRNA gene-expression data set used the publicly available GSE47460 data set. The 159-mRNA gene expression data set contained data from $n = 121$ individuals with COPD, $n = 20$ non-smokers and $n = 18$ smokers with phenotypic information along with LTRC overall final pathologic diagnosis (CPAL1) is presented in Supplementary Table 2.

Distributional location of the lung tissue resection (right or left, upper or lower lobe), along with pathological diagnosis is presented in Supplementary Table 3.

Validation of mitochondrial genes in two COPD cohorts. To compare the mitochondrial genes in human COPD lung tissue with high or low IRP2 expression that we identified, we used two independent COPD cohort data sets of gene expression.

COPD data set 1. We used publicly available gene expression data from the LGRC (<http://www.ncbi.nlm.nih.gov/geo/query/acc.cgi?acc=GSE47460>). Data collected using each of the two array platforms included was background-corrected and then normalized between arrays using limma⁸⁴. Next we removed duplicate probes and then merged the two array platforms by matching probes that shared the same gene name. This merged data set was then corrected for array-specific batch effects using ComBat⁸⁵. Of the 580 subjects included in this publicly available data, we identified those with a COPD diagnosis or a control status (219 and 107 individuals, respectively). Approximately half of these subjects were subsequently removed based on quality control, leaving us with a 159-subject mRNA gene-expression data set contained ($n = 121$ COPD, $n = 20$ non-smokers and $n = 18$ smokers). In this final data set, all subjects with COPD had a DLCO less than 80%, and all controls (both smokers and non-smokers) had a DLCO greater than 80%.

COPD data set 2. We also used gene expression data from the ECLIPSE (Evaluation of COPD Longitudinally to Identify Predictive Surrogate End-points) study. This study was a 3-year observational study⁸⁶, where emphysema-predominant COPD was defined by $>10\%$ of lung voxels with attenuation ≤ -950 HU (Hounsfield units) on inspiratory chest CT scans.

Other assessments include pulmonary function measurements (spirometry, impulse oscillometry, chest computed tomography, biomarker measurement (in blood, sputum, urine and exhaled breath condensate), health outcomes, body impedance, resting oxygen saturation and 6-min walking distance⁸⁶). CEL expression files from ECLIPSE (GSE54837), with phenotype information, was downloaded from GEO (<http://www.ncbi.nlm.nih.gov/geo/geo2r/?acc=GSE54837>)⁸⁶. This particular data set contained $n = 136$ COPD subjects, $n = 84$ smoker controls, $n = 6$ non-smoker controls. The ECLIPSE data was RMA-normalized using a custom CDF.

Raw expression data from the two COPD cohorts was downloaded, including raw data files (.TAR) from LGRC (GSE47460), and CEL expression files from ECLIPSE (GSE54837); the ECLIPSE data was RMA-normalized using a custom CDF. We identified which of our selected mitochondrial genes (Fig. 3a) were measured in each of these cohorts and showed their expression levels in ECLIPSE and LGRC (Fig. 3b,c and Supplementary Fig. 6) within different subject populations. In each heat map, the subjects are ordered (from left to right) based on increasing values of *IRP2* gene expression, with a white bar delimiting which individuals were identified as having low *IRP2* expression (less than the median across all subjects) or high *IRP2* expression (greater than the median across all subjects). Rows are ordered the same as Figure 3a and each row is z-score-normalized for visualization purposes (Supplementary Fig. 6).

For the LGRC gene-expression data set, the overall 'meta' P values (for the genes in the heat map) were: COPD subjects: 1.4×10^{-3} ; smoker controls: 0.9564; non-smoker controls: 0.5303 (Supplementary Fig. 6a). For the ECLIPSE data set, the overall meta P values (for the genes in the heat map) were: COPD subjects: 1.4088×10^{-7} ; smoker-controls: 6.1838×10^{-3} ; non-smoker controls: 1.6108×10^{-5} (Supplementary Fig. 6b). In all cases the overall differential expression is consistent with observations in the *Irp2*^{-/-} versus WT mice (overall decreased expression of these genes in low *IRP2* as compared to high *IRP2*, corresponding to more green on the left of the heat maps).

Finally, we also compared our results with a study published earlier that defined a 127-gene expression signature associated directly with increases in L_m from microCT information of COPD subjects as reported by Campbell *et al.*⁸⁷. While *IRP2* was not enriched in the 127-gene expression list in Campbell *et al.*⁸⁷, it had an FDR of <1 (0.63) and a t -statistic of -1.44. On this list, *IRP2* (*IREB2*) was ranked 2,475 (out of 17,879), based on the fold change value, and 2,282 (out of 17,879), based on the t -statistic value. When we examined the 127-gene expression signature from Campbell *et al.* for gene targets that were common to our RIP-seq study, we noted that 114 of the genes in this expression signature were included in the annotations used by HOMER, when mapping our peak calls. Of these 114 genes, 27 had an identified *IRP2* peak in our data, an overlap that is marginally significant ($P = 0.06$, Fisher's Exact test). When investigating the three sets of peaks separately (CTRL, DFO, and common), there was a strong significant overlap (18 genes, $P = 1.6 \times 10^{-3}$) between the 127 genes in the expression signature and the genes that had common peaks of *IRP2*. Furthermore, within the set of 27 genes in the gene expression signature that also had an identified *IRP2* peak, there was a relative enrichment for genes with decreased expression with increased emphysema severity (21/27 or 78% of genes in the expression signature that have an *IRP2* peak have decreased expression with increased emphysema severity, as compared to 73/114 or 64% of all genes in the full expression signature). This was highly driven by genes with peak calls in the DFO experiment; all 12 genes in the gene-expression signature that had a DFO peak were found to have decreased expression levels with increased emphysema severity.

Human samples and study approval. Human lung tissues were analyzed under the guidelines of Brigham and Women's Hospital Institutional Review Board (IRB) approval. Human samples were classified based on the guidelines of the Global Initiative for Obstructive Lung Disease (GOLD2) as previously described^{17,18,22}. Human samples obtained from the Lung Genomics Tissue Research Consortium (LTRC) used in Figure 5a were homogenates from GOLD2 tissues obtained from open lung biopsies and are described in Supplementary Table 4 (adapted from Lam *et al.*¹⁸). The Lung Genomics Research Consortium (LGRC) provides genetic, molecular, and quantitative phenotype data for human samples in the National Heart, Lung and Blood Institute LTRC biorepository

(<http://www.lung-genomics.org>). Informed consent was obtained from all subjects included in these studies.

Transmission electron microscopy (TEM). Tissues from mice exposed to chronic CS were fixed overnight at 4 °C using TEM-grade fixative solution of 2% formaldehyde and 2.5% glutaraldehyde in 0.1 M sodium cacodylate buffer, pH 7.4. The samples were washed and stored in 0.1 M sodium cacodylate buffer and kept at 4 °C until processing. Sample embedding was performed using a standard protocol as previously described¹⁸. For EM quantification, 15 image fields were selected at random by a blinded reader for each mouse or sample ($n = 1$ mouse per group). Specifically, a blinded code was generated by the TEM core facility and images were acquired by an experienced core facility technician. S.M.C. analyzed slides using a blinded key. The total area of the cytoplasm was calculated, and the number of mitochondria with 'abnormal' characteristics (defined as mitochondria with swollen or abnormal cristae) per unit area of cytoplasm were counted using ImageJ (NIH).

Cell culture, siRNA, shRNA and CSE. Primary epithelial cells were isolated from mouse lungs as previously described and used for experiments before passage¹⁷. Primary human bronchial epithelial (HBE) cells were obtained from the American Type Culture Collection (ATCC) and were cultured according to ATCC's instructions. Human lung bronchial epithelial Beas-2B cells were purchased from ATCC and maintained in Dulbecco's modified Eagle's medium (DMEM) containing 10% FBS and gentamicin (100 µg/ml). Beas2B and HBE cell lines were authenticated and checked for mycoplasma infection. Beas2B cells were treated with siRNA targeted to human *IRP2* (SMARTpool: ON-TARGETplus *IREB2* siRNA L-022281, Dharmacon, GE Healthcare) for 48 h using Lipofectamine RNAiMAX Transfection Reagent (Life Technologies) using standard transfection techniques. shRNA targeted to human *IREB2* was from Sigma-Aldrich (NM_004136, iron-responsive element-binding protein 2 MISSION shRNA). MISSION shRNA clones in shRNA lentiviral plasmids (pLKO.1-puro) were purchased as frozen bacterial glycerol stocks in *Escherichia coli* for propagation and downstream purification of the shRNA clones. shRNA viral particles were generated using standard procedures, and cells containing positive shRNA clones were selected for using puromycin.

CSE was prepared and added to culture media as previously described^{63,88}. Briefly, a peristaltic pump (VWR International) was used to bubble mainstream smoke from five 3R4F cigarettes with filters removed through 50 ml DMEM. Each cigarette was smoked within 6 min until approximately 17 mm remained. The extract was filter-sterilized, stored at -80 °C, and used immediately upon thawing. The CSE generated in this fashion was considered to be at 100% strength and was diluted in complete DMEM medium for cell treatment.

Measurement of mitochondrial membrane potential and cytochrome c oxidase activity. Mitochondria-enriched fractions were isolated from the lungs of mice and JC1 uptake was measured by using the MITOISO1 mitochondrial isolation kit (Sigma-Aldrich). Mitochondrial membrane potential was measured in primary epithelial cells using tetramethylrhodamine ethyl ester (TMRE) (Abcam). Briefly, cells were treated with CSE or 20 µM carbonylcyanide *p*-trifluoromethoxyphenylhydrazone (FCCP) for the indicated times and stained for 20 min at 37 °C with 150 nM TMRE. Data were acquired with a FACSCanto II (BD Biosciences) and analyzed with FlowJo analytical software (Tree Star Inc.). Cytochrome c oxidase activity was measured in mitochondria-enriched fractions using an optimized colorimetric assay based on the decrease in absorbance of ferrocytochrome *c* measured at 550 nm, which is caused by its oxidation to ferricytochrome *c* by cytochrome *c* oxidase (Sigma-Aldrich).

Seahorse analysis. Extracellular acidification rates and oxygen consumption rates were determined by the Seahorse XF 96 flux analyzer (Seahorse Bioscience). Primary airway epithelial cells were isolated as described above and plated onto cell culture microplates (Seahorse Bioscience) coated with 50 ng/µl laminin 1 (3400-010-01, Trevigen) for 4 d (with medium change on day 2). On the day of the experiment, cells were treated with CSE for 4 h. Cells were incubated in XF assay medium (Seahorse Bioscience), supplemented with 5 mM glucose, 4 mM glutamine and 1 mM pyruvate for 1 h before the measurement. After the recording of the basal rates of ECAR and OCR, final concentrations of 1 µM

oligomycin, 2 μM FCCP and 0.5–0.5 μM rotenone and antimycin A were added (Sigma) through the instrument's injection ports to obtain proton leak, maximal respiratory capacity and non-mitochondrial respiration, respectively. Rates were normalized by DNA with Hoechst 33342 against standards with known concentrations of DNA.

Perls' stain and non-heme iron measurements. Formalin-fixed, paraffin-embedded 5- μm -thick lung sections were deparaffinized through graded alcohols and washed in PBS. Slides were incubated in Perls' stain (5% potassium ferrocyanide with 5% hydrochloric acid) for 30 min at RT. 500 μl of nuclear fast-red solution was added to each slide and incubated for 4 min. Slides were dehydrated using graded alcohols and samples viewed by a blinded experienced reader using a light microscope (Axiophot; Carl Zeiss MicroImaging) equipped with a digital camera (Axiocam HRC; Carl Zeiss MicroImaging) at 200 \times magnification. Perls' stain reacts with iron to form a blue-black color. Staining was quantified in $n = 3$ or 4 mice per group ($n = 10$ 20 \times images per mouse) by a blinded experienced reader and staining quantified using the Threshold feature in ImageJ. Lung sections were blinded by taping the slide identifiers before acquiring images and before data analysis. Random-number generations using excel and a gridded coverslip were used to choose the sample image area for acquisition in all cases.

Non-heme iron assay. Lung tissue (50–200 mg) or 50- to 200- μl subcellular fractions were incubated with 100–500 μl of NHI Acid (10% trichloroacetic acid in 3 M HCl) overnight at 65 $^{\circ}\text{C}$. Samples were cooled, vortexed and centrifuged at 2,000 r.p.m. for 15 s. Equal volumes of sample or iron standard (25–0.39 $\mu\text{g}/\text{ml}$ using NHI Acid) were incubated in a 1-ml cuvette for 5–10 min at RT with 800 μl BAT Buffer (0.2% thioglycolic acid, 0.02% bathophenanthroline sulfonate in 1/2 saturated NaAc solution). Samples were read at 535 nm, and unknowns were calculated from a standard curve.

Heme iron assay. Heme iron was measured in isolated mitochondrial and cytosolic fractions using the QuantiChrom Heme Assay Kit (BioAssay Systems) according to the manufacturer's instructions. Briefly, heme iron was measured in 10 μl of mitochondrial or cytosolic fractions by measuring the intensity obtained at 400 nm against a standard curve of known concentrations of heme.

Measurement of labile iron pool using calcein-AM (CA-AM). The labile iron pool of Beas2B cells was measured as previously described⁸⁹. Briefly, 10⁶ Beas2B cells were seeded in a 10-cm dish, left overnight, harvested by trypsinization, counted and resuspended in serum-free DMEM. Cells were incubated with 0.5 μM CA-AM at 37 $^{\circ}\text{C}$ for 8 min with constant agitation before washing with Hanks' Balanced Salts (HBS) solution (containing phenol red). Cells were resuspended in HBS and incubated with trypan blue (25 μg) to block extracellular fluorescence. Fluorescence was measured at 517-nm emission and 488-nm excitation, measuring the blank rate before the addition of 100 μM salicylaldehyde isonicotinoyl hydrazine (SIH). The change in fluorescence (ΔF) upon SIH addition was calculated for each sample. In cells without trypan blue, a series of increasing concentrations of calcein were added sequentially and the ΔF was calculated to construct a calcein versus ΔF standard curve.

Immunoblotting. Immunoblot analyses were performed in whole-lung homogenates or mitochondria-enriched fractions isolated from the lungs of mice using standard immunoblotting techniques with the following antibodies to the following proteins: Irp2 (1:1,000 7H6: sc-33682, 1:1,000 Santa Cruz, NB100-1798, Novus Biologicals and Irp2 antibody from T.A.R. at a 1:1,000 dilution), Irp1 (1:1,000 NBP1-19412, aconitase 1 antibody, Novus Biologicals), LC3B (1:2,000 L7543, Sigma-Aldrich), Atg7 (1:2,000 APG7 (H-300): sc-33211, Santa Cruz), transferrin receptor 1 (1:1,000 CD71 (H-300): sc-9099, Santa Cruz), actin (1:10,000 A00158, Sigma-Aldrich), electron transport chain components including COX MTCO1 (1:500 MitoProfile Total OxPhos antibody, ab110413, Abcam), ferritin (1:1,000 H-53: sc-25617, Santa Cruz), Tom20 (1:2,000 FL-145, sc-11415, Santa Cruz), frataxin (1:1,000 H-155: sc-25820, Santa Cruz), mitoferrin 2 (1:1,000 P-12: sc-138430, Santa Cruz), cleaved caspase-3 (1:500 Asp175, Cell Signaling Technology), Bcl2 (1:1,000 sc-7382, Santa Cruz), Fbxl5 (1:1,000 N0039, Neoclone Biotechnology) Cox4i2 (1:1,000 H00084701-M01 Abnova) and HO-1 (1:1,000 sc-1797, Santa Cruz).

Real-time qPCR. mRNA was extracted from lung tissue using the Qiagen RNA extraction kit (74104, Qiagen) and reverse-transcribed with SuperScript III

Reverse Transcriptase (Life Technologies). TaqMan primers for gene-expression assays were purchased from Life Technologies. Real-time qPCR was carried out with an ABI PRISM 7300 Sequence Detection System using TaqMan PCR Master Mix (Life Technologies). mRNA was extracted from cells using the Qiagen RNA extraction kit (74104, Qiagen) and reverse-transcribed with SuperScript III Reverse Transcriptase (Life Technologies). The mRNA in **Supplementary Figure 4f** was used from RIP-seq library preparations. TaqMan primers for human transferrin receptor 1, human ferritin heavy chain, human frataxin and human β -actin for gene-expression assays were purchased from Life Technologies. Real-time qPCR was carried out with an ABI PRISM 7300 Sequence Detection System using TaqMan PCR Master Mix (Life Technologies).

Flow cytometry. To discriminate between live and dead cells, cells were simultaneously stained with green fluorescent calcein-AM to indicate intracellular esterase activity and red fluorescent ethidium homodimer-1 to indicate loss of plasma membrane integrity using the LIVE/DEAD Viability/Cytotoxicity Kit (L-3224, Molecular Probes). mtROS was measured in cells by MitoSOX (M36008, Invitrogen) staining (2.5 μM for 10 min at 37 $^{\circ}\text{C}$). Data were acquired with a FACSCanto II (BD Biosciences) and analyzed with FlowJo analytical software (Tree Star Inc.).

Confocal imaging. 80,000 Beas2B cells seeded onto poly-L-lysine-coated cover slips in a 6-well plate were treated with CSE for the indicated times. The cells were permeabilized for 15 min in 0.01% Triton-X 100 then washed in PBS twice and 0.5% bovine serum albumin (BSA) in PBS twice. The cells were blocked for 45 min with 2% BSA in PBS. The cells were washed once in 0.5% BSA and then incubated for 1 h at room temperature with a primary rabbit IgG to human IRP2 (1:100, sc-33682, Santa Cruz). The samples were washed five times with 0.5% BSA and then incubated for 1 h at room temperature in secondary IgG Alexa 488 anti-rabbit antibody (1:400). Nuclei were stained using DAPI.

Measurement of Fe-S cluster assembly in Beas2B cells. 2Fe-2S clusters were measured in Beas2B cells as previously described⁹⁰. Briefly, 8×10^5 Beas2B cells were transfected with constructs (0.8 μg) containing Venus fluorescent protein fragments targeted to the mitochondrion or cytosol and conjugated to human glutaredoxin 2 (GRX2), which coordinates 2Fe-2S clusters, for 24 h. Transfected cells were treated with 20% CSE for 0.5, 1 or 2 h. The fluorescence of cells transiently transfected with vectors that express the mitochondrial and cytosolic Venus fragment pairs fused to GRX2 was determined using flow cytometry (measuring FITC fluorescence). The fluorescence of Venus fragments fused to the self-associating leucine-zipper region of the yeast Gcn4 transcriptional activator were used as a control for Venus fragments that stably associate (data not shown).

Statistical analysis. Statistical analysis was conducted using GraphPad Prism software (GraphPad Software). Data are presented as the mean \pm s.e.m. from at least two independent experiments. Differences in measured variables between experimental and control groups were assessed using the unpaired Student's *t*-test and between multiple groups and conditions using one-way and two-way ANOVAs with subsequent Bonferroni-corrected pairwise tests. For MCC assays, a significant *P* value was followed by a pair-wise comparison using a two-sample *t*-test for a priori hypotheses only. Thus, no adjustment in the significance level was made for multiple comparisons. Multivariable regression was conducted using STATA/IC (v13) to isolate the effects of IRP2, C:P ratio, DFP, CS, and iron diets (**Fig. 6a,c**). *P* values were calculated, and minimum statistical significance was accepted at *P* < 0.05. Mean values appeared to be normally distributed, with each figure documenting an appropriate statistical test. For animals subjected to cigarette smoke exposure, early death was used as an exclusion criterion. However, only one mouse died out of all of those exposed in CS-exposure studies.

61. Lee, P.J. *et al.* Regulation of heme oxygenase-1 expression *in vivo* and *in vitro* in hyperoxic lung injury. *Am. J. Respir. Cell Mol. Biol.* **14**, 556–568 (1996).

62. Siempos, I.I. *et al.* Cecal ligation and puncture-induced sepsis as a model to study autophagy in mice. *J. Vis. Exp.* **84**, e51066 (2014).

63. Chen, Z.H. *et al.* Autophagy protein microtubule-associated protein 1 light chain-3B (LC3B) activates extrinsic apoptosis during cigarette smoke-induced emphysema. *Proc. Natl. Acad. Sci. USA* **107**, 18880–18885 (2010).
64. Parameswaran, H., Majumdar, A., Ito, S., Alencar, A.M. & Suki, B. Quantitative characterization of airspace enlargement in emphysema. *J. Appl. Physiol.* **100**, 186–193 (2006).
65. Laucho-Contreras, M.E., Taylor, K.L., Mahadeva, R., Boukedes, S.S. & Owen, C.A. Automated measurement of pulmonary emphysema and small-airway remodeling in cigarette smoke-exposed mice. *J. Vis. Exp.* **95**, e52236 (2015).
66. Jacob, R.E. *et al.* Comparison of two quantitative methods of discerning airspace enlargement in smoke-exposed mice. *PLoS One* **4**, e6670 (2009).
67. Jacob, R.E., Minard, K.R., Laicher, G. & Timchalk, C. 3D ³He diffusion MRI as a local *in vivo* morphometric tool to evaluate emphysematous rat lungs. *J. Appl. Physiol.* **105**, 1291–1300 (2008).
68. Wilson, A.A. *et al.* Amelioration of emphysema in mice through lentiviral transduction of long-lived pulmonary alveolar macrophages. *J. Clin. Invest.* **120**, 379–389 (2010).
69. Hamakawa, H. *et al.* Structure-function relations in an elastase-induced mouse model of emphysema. *Am. J. Respir. Cell Mol. Biol.* **45**, 517–524 (2011).
70. Summer, R. *et al.* Alveolar macrophage activation and an emphysema-like phenotype in adiponectin-deficient mice. *Am. J. Physiol. Lung Cell. Mol. Physiol.* **294**, L1035–L1042 (2008).
71. Nobuyuki, O. A threshold selection method from gray-level histograms. *IEEE Trans. Syst. Man Cybern. Syst.* **9**, 62–66 (1979).
72. Soille, P. in *Morphological Image Analysis: Principles and Applications* (Springer-Verlag, Berlin, Heidelberg) 170–171 (1999).
73. Meyer, F. Topographic distance and watershed lines. *Signal Processing* **38**, 113–125 (1994).
74. Kuhn, C. 3rd *et al.* Airway hyper-responsiveness and airway obstruction in transgenic mice. Morphologic correlates in mice overexpressing interleukin (IL)-11 and IL-6 in the lung. *Am. J. Respir. Cell Mol. Biol.* **22**, 289–295 (2000).
75. Bhashyam, A.R. *et al.* A pilot study to examine the effect of chronic treatment with immunosuppressive drugs on mucociliary clearance in a vagotomized murine model. *PLoS One* **7**, e45312 (2012).
76. Mortensen, J., Lange, P., Nyboe, J. & Groth, S. Lung mucociliary clearance. *Eur. J. Nucl. Med.* **21**, 953–961 (1994).
77. Goforth, J.B., Anderson, S.A., Nizzi, C.P. & Eisenstein, R.S. Multiple determinants within iron-responsive elements dictate iron-regulatory protein binding and regulatory hierarchy. *RNA* **16**, 154–169 (2010).
78. Dai, M. *et al.* Evolving gene/transcript definitions significantly alter the interpretation of GeneChip data. *Nucleic Acids Res.* **33**, e175 (2005).
79. Dennis, G. Jr. *et al.* DAVID: Database for annotation, visualization and integrated discovery. *Genome Biol.* **4**, 3 (2003).
80. Huang, W., Sherman, B.T. & Lempicki, R.A. Bioinformatics enrichment tools: paths toward the comprehensive functional analysis of large gene lists. *Nucleic Acids Res.* **37**, 1–13 (2009).
81. Clauset, A., Newman, M.E. & Moore, C. Finding community structure in very large networks. *Phys. Rev. E* **70**, 066111 (2004).
82. Oron, A.P., Jiang, Z. & Gentleman, R. Gene set-enrichment analysis using linear models and diagnostics. *Bioinformatics* **24**, 2586–2591 (2008).
83. Blake, J.A. *et al.* Gene Ontology Consortium. Gene Ontology annotations and resources. *Nucleic Acids Res.* **41**, D530–D535 (2013).
84. Smyth, G.K. *Bioinformatics and Computational Biology Solutions Using R and Bioconductor* (Springer, New York, 2005).
85. Johnson, W.E., Li, C. & Rabinovic, A. Adjusting batch effects in microarray expression data using empirical Bayes methods. *Biostatistics* **8**, 118–127 (2007).
86. Vestbo, J. *et al.* ECLIPSE investigators. Evaluation of COPD longitudinally to identify predictive surrogate end points (ECLIPSE). *Eur. Respir. J.* **31**, 869–873 (2008).
87. Campbell, J.D. *et al.* A gene-expression signature of emphysema-related lung destruction and its reversal by the tripeptide GHK. *Genome Med.* **4**, 67 (2012).
88. Chen, Z.H. *et al.* Egr-1 regulates autophagy in cigarette smoke-induced chronic obstructive pulmonary disease. *PLoS One* **3**, e3316 (2008).
89. Epsztejn, S., Kakhlon, O., Glickstein, H., Breuer, W. & Cabantchik, I. Fluorescence analysis of the labile iron pool of mammalian cells. *Anal. Biochem.* **248**, 31–40 (1997).
90. Hoff, K.G. *et al.* *In vivo* fluorescence detection of Fe-S clusters coordinated by human GRX2. *Chem. Biol.* **16**, 1299–1308 (2009).